

A spatio-temporal active-fire clustering approach for global burned area mapping at 250 m from MODIS data

Joshua Lizundia-Loiola*, Gonzalo Otón, Rubén Ramo, Emilio Chuvieco

Environmental Remote Sensing Research Group, Department of Geology, Geography and the Environment, Universidad de Alcalá, Calle Colegios 2, Alcalá de Henares, 28801, Spain



ARTICLE INFO

Keywords:

MODIS
Burned area mapping
Algorithm
Active fire

ABSTRACT

This paper presents the generation of a global burned area mapping algorithm using MODIS hotspots and near-infrared reflectance within ESA's Fire_cci project. The algorithm is based on a hybrid approach that combines MODIS highest resolution (250 m) near-infrared band and active fire information from thermal channels. The burned area is detected in two phases. In the first step, pixels with a high probability of being burned are selected in order to reduce commission errors. To do that, spatio-temporal active-fire clusters are created to determine adaptive thresholds. Finally, a contextual growing approach is applied from those pixels to the neighbouring area to fully detect the burned patch and reduce omission errors. The algorithm was used to obtain a time series of global burned area dataset (named FireCCI51), covering the 2001–2018 period. Validation based on 1200 sampled sites covering the period from 2003 to 2014 showed an average omission and commission errors of 67.1% and 54.4%. When using longer validation periods, the errors were found smaller (54.5% omission and 25.7% commission for the additional 1000 African sampled sites), which indicates that the product is negatively influenced by temporal reporting accuracy. The inter-comparison carried out with previous Fire_cci versions (FireCCI41 and FireCCI50), and NASA's standard burned area product (MCD64A1 c6) showed consistent spatial and temporal patterns. However, the new algorithm estimated an average BA of 4.63 Mkm², with a maximum of 5.19 Mkm² (2004) and a minimum of 3.94 Mkm² (in 2001), increasing current burned area estimations. Besides, the new product was found more sensitive to detect smaller burned patches. This new product, called FireCCI51, is publicly available at: <http://cci.esa.int/data>, last accessed on September 2019.

1. Introduction

Throughout history, humans have used fire as an environmental management tool, either for reducing the amount of biomass present on the landscape or control wild flora and fauna (Bird and Cali, 1998; Bowman et al., 2009). Vegetation characteristics, mainly biomass loads and moisture, determine fire behaviour (Archibald et al., 2013; Hantson et al., 2016), but fire also modifies vegetation structure and evolution (Bond and Keeley, 2005). Climate affects fire occurrence through the thermal and precipitation cycles, but it is also affected by fire, particularly by gaseous and PM emissions (Forkel et al., 2017). This mutual influences among vegetation, climate and fire highlight the importance of having global long-term burned area (BA) information that serves as input for climate and vegetation modellers (Mouillot et al., 2014; Seiler and Crutzen, 1980; van der Werf et al., 2017). For this reason, fire disturbance is considered an Essential Climate Variable (ECV) by the Global Climate Observing System (GCOS) program (Bojinski et al.,

2014; Mason et al., 2010). This program encourages generating long-term time series (> 30 years) of ECVs data, which should complement ground sensors and climate models to better understand climate trends. This interest has led the space agencies to develop ECV products from satellite observations at different spatial and temporal scales (Hollmann et al., 2013). Within this scope, several international programs aim to generate global BA products that may serve the needs of climate and atmospheric modellers (Mouillot et al., 2014).

Global BA products have been available only in the last decades. A recent review on historical and current developments of satellite observation of BA shows the progression of BA algorithms, from a single year and regional products to multi-annual and global ones (Chuvieco et al., 2019).

The first BA products derived from satellite data were generated from the National Oceanic and Atmospheric Administration's Advanced Very High Resolution Radiometer (NOAA-AVHRR) sensor in the late '80s. These studies aimed to detect BA for relatively small regions (< 3

* Corresponding author.

E-mail address: joshua.lizundia@uah.es (J. Lizundia-Loiola).

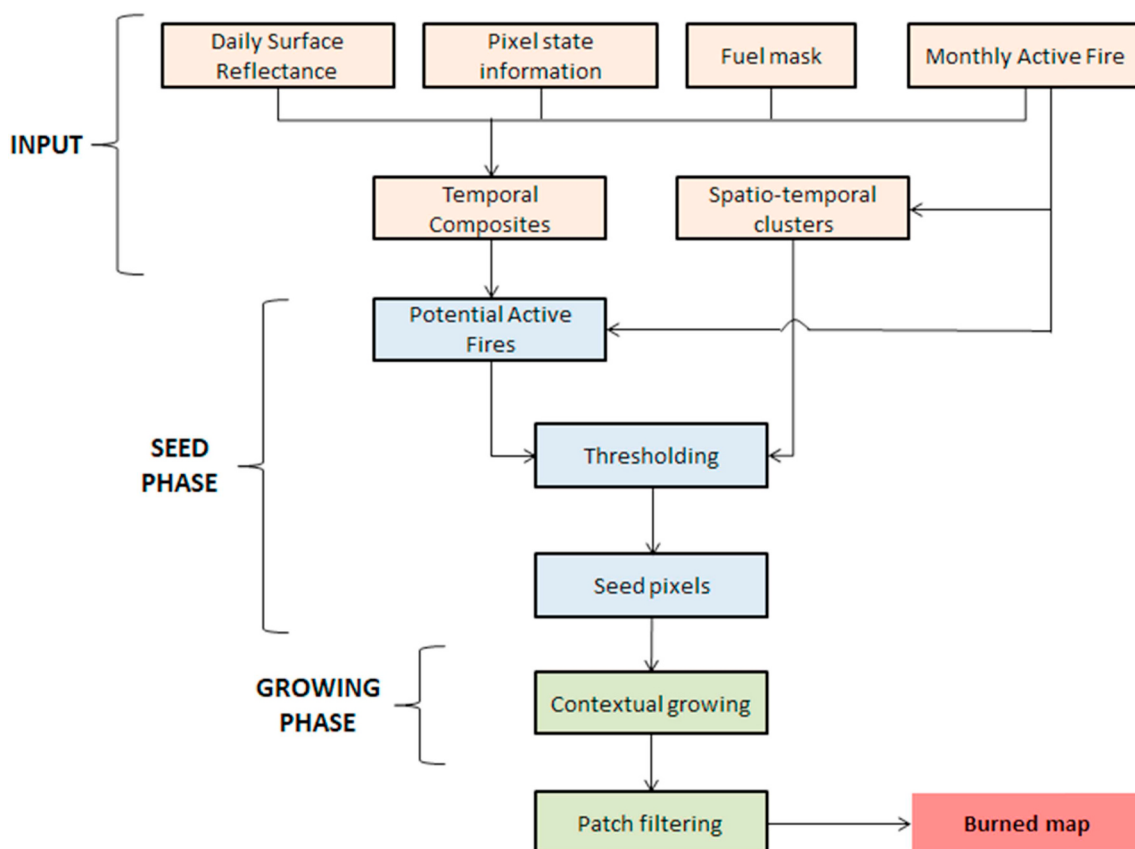


Fig. 1. Main steps of the algorithm: input, seed and growing phase.

Mkm²) and were based on dedicated algorithms, with unknown accuracy for other regions (Kasischke and French, 1995; Roy et al., 1999).

When the first attempts to generate global products were proposed in the early 2000s, they were based on different regional algorithms as well. This was the case of the GBA2000 project (Tansey et al., 2004), which used nine regional algorithms created by different institutions based on Systeme Pour l'Observation de la Terre 4 – VEGETATION's (SPOT-VGT) surface reflectance data. Most of those algorithms used the near-infrared (NIR) reflectance (Silva et al., 2002; Stroppiana et al., 2003) or both NIR and short-wave infrared (SWIR) bands (Boschetti et al., 2002), but another one used the Normalized Difference Vegetation Index (NDVI) (Fraser et al., 2003). As the criteria to detect BA were quite different in diverse regions, the final product was found inconsistent as well. For this reason, the successor project, aiming to map BA for a longer time series, decided to process a single algorithm named L3JRC (Tansey et al., 2008). This algorithm was based on the detection of abrupt changes in NIR reflectance (Ershov and Novik, 2001). A blending of two algorithms was also used in the GLOBSCAR project of the European Space Agency (ESA), which was based on the NIR, SWIR and thermal infrared (TIR) bands of the Along Track Scanning Radiometer (ATSR-2) sensor (Simon et al., 2004).

The launching of NASA's Moderate Resolution Imaging Spectroradiometer (MODIS) aboard Terra (launched 1999) and Aqua (launched 2002) satellites provided additional opportunities to develop global BA products. Two global BA products have been generated from these data: the MCD45 and MCD64, although nowadays only the latter is routinely processed. These two products are based on different algorithms. The MCD45 (Roy et al. 2002, 2005) compares daily modelled reflectance, which is derived from a physical-based Bi-directional Reflectance Distribution Function (BRDF) model, with actual reflectance of bands 2 (NIR 841–876 nm) and 5 (SWIR 1230–1250 nm). On the other hand, the MCD64 (Giglio et al. (2009), updated in Giglio et al.

(2018)) uses a hybrid approach, combining active fires with changes in a vegetation index generated from bands 5 and 7 (SWIR 2105–2155 nm). Both products offer BA information at 500 m resolution for the years, 2001–2016 and 2001–present, respectively. The MCD64 product also feeds the Global Fire Emission Database (GFED), widely used to estimate fire emissions (van der Werf et al., 2017).

As part of the ESA Climate Change Initiative programme, the Fire_cci project (<https://www.esa-fire-cci.org/>, last accessed on September 2019) produced new global BA products, based on the European sensor MERIS and the highest resolution channels of MODIS (at 250 m). The former covers the period from 2005 to 2011 (named FireCCI41: Chuvieco et al. (2016)) and the latter the period from 2001 to 2016 (FireCCI50: Chuvieco et al. (2018)). Both follow a two-phase hybrid approach that made use of thermal anomalies provided by MODIS and the spectral behaviour of burned patches in the Red-NIR region (Alonso-Canas and Chuvieco, 2015; Chuvieco et al. 2016, 2018). Although FireCCI50 showed a better performance than FireCCI41 (13% improvement in commission error and 10% in omission error), results still presented high commission and omission errors, similar to other global BA products (Chuvieco et al., 2018). In a smaller proportion than in FireCCI41, three main issues were found that negatively affected FireCCI50's accuracy: border effects on fires placed in the borders of the tiles, low-intensity fire detection problems, and excessive growing. However, MODIS at 250 m resolution showed a higher potential to detect BA than MERIS and showed a higher sensitivity to small fires than other global BA products (Chuvieco et al., 2018).

The main objective of this paper is to present the new version of a global BA algorithm developed within the Fire_cci project that tries to overcome problems found in the previous version. The algorithm is still based on MODIS 250 m reflectance bands, guided by active fire information, and uses a two-phase approach (seed detection + region growing). However, it develops a new concept of burned area detection

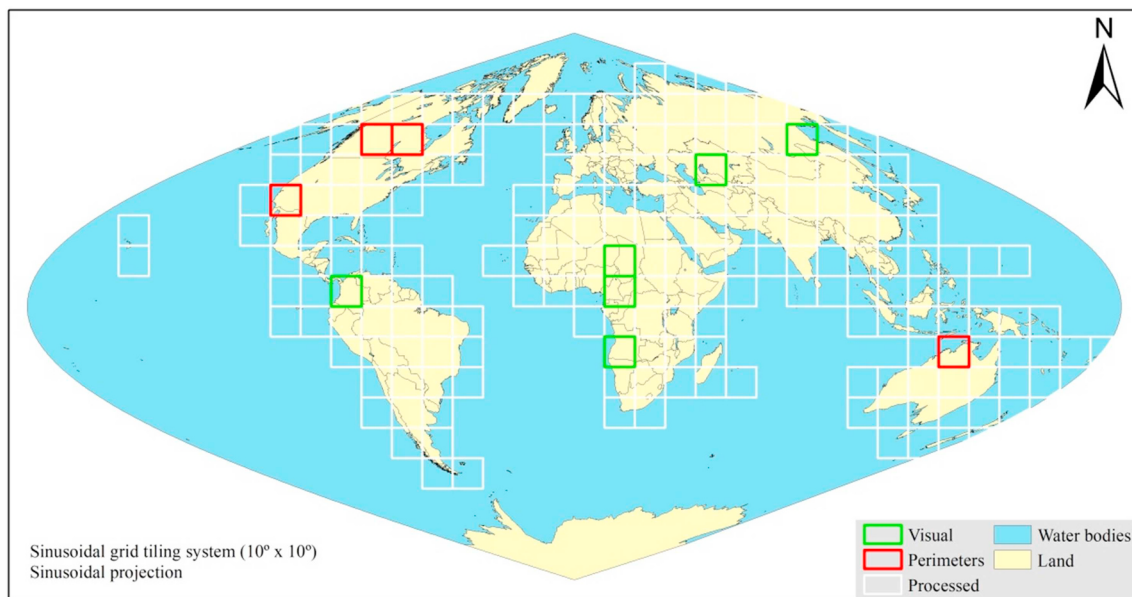


Fig. 2. Processed and calibrated tiles.

based on region-based thresholding, which we hypothesized would be better adapted to seed detection and growing phases for different vegetation covers than tile-based thresholds. The manuscript describes the different phases of the algorithm and presents the results of the BA detections for the full time series of MODIS data (2001–2018). Validation was based on a multi-temporal stratified random sampling of reference perimeters derived from Landsat data.

2. Methods

2.1. Algorithm structure

The structure of the BA algorithm is presented in Fig. 1. Our approach follows a hybrid approach, using both thermal anomalies information and near-infrared reflectance values. Thermal anomalies were used to identify active fires, as they have high thermal contrast with the background (Giglio et al., 2016). However, thermal anomalies only detect burnings at the time of the satellite overpass, providing only a sample of the total BA (Giglio et al., 2006; Hantson et al., 2013). The change in reflectance is temporally more persistent, but it presents potential confusion with other cover changes such as floods, snowmelt or harvesting, particularly in dark soils (Alonso-Canas and Chuvieco, 2015; Roy et al., 2005). Hybrid algorithms combine the strengths of thermal and reflectance changes to discriminate burned areas. The first hybrid approaches mixed thermal and reflectance channels to create spectral indices that were more sensitive to burned areas, including the near-infrared and the reflectance component of the middle infrared (Kaufman and Remer, 1994). The combination of active fires and reflectance changes was first proposed by Roy et al. (1999) to guide the detection thresholds of spectral indices using AVHRR images. Later, active fires were used to confirm potential burned patches that were detected using change detection techniques (Fraser et al., 2000). More elaborated algorithms were developed by Giglio et al. (2009, 2018), using active fires and land cover information to guide the statistical characterization of BA based on MODIS data. Alonso-Canas and Chuvieco (2015) discriminated BA applying a two-phase approach (seed + growing) that used tile-based thresholds from MERIS reflectance values and MODIS active fires. Chuvieco et al. (2018) adapted the same ideas to MODIS 250 m data, while introducing additional rules to better locate the active fires and establishing regional thresholds for both phases of the BA detection.

Following previous experiences of our group (Alonso-Canas and Chuvieco, 2015; Bastarrika et al., 2011; Chuvieco et al., 2008), the new algorithm used a two-phase methodology (Fig. 1). First, pixels that have a high probability of being burned, called ‘seeds’, were chosen using restrictive spectral conditions (to reduce commission errors). Those candidate ‘seed’ pixels were derived from MODIS thermal anomalies considering the relative drop in NIR reflectance. Then a contextual region growing was applied from the ‘seeds’ to entirely detect the burned patch, in order to reduce the omission errors. Before selecting the seeds, monthly temporal NIR composites were created to reduce noise caused by clouds, cloud shadows, and different artefacts. Two variables were used for BA detection: NIR post-fire values, given by the monthly composites, and the relative change between consecutive NIR composites values.

The algorithm presented in this paper advances from previous BA hybrid algorithms by introducing cluster-based thresholds, in both the seed and region-growing phases. This is the main novelty of this algorithm, which identifies burned-unburned thresholds of reflectance from values of spatially-aggregated active fires and its surroundings. Unlike tile-based thresholding methods, this approach allows obtaining adaptive thresholds for different vegetation covers within the same tile. In addition, thresholds are not dependent on land cover information and, therefore, the uncertainties associated with land cover classification are removed.

The following paragraphs describe in detail the different phases of the BA algorithm. Table 2 at the end of this description includes a summary of the parameters selected for each phase. They were derived from previous studies or empirically generated from the different calibration sites. A sensitivity analysis of these empirical values is also presented in section 2.9.

As in other MODIS based BA algorithm processing (Giglio et al., 2018; Roy et al., 2005), the computational units were the MODIS standard tiles of about 1200×1200 km (4800×4800 pixels) and sinusoidal projection. A total of 210 tiles covering all main burnable areas of the Earth were processed (Fig. 2) to obtain the full time series of MODIS data (2001–2018). The output product was named FireCCI51, which includes pixel and grid BA values on a monthly basis. The product is freely downloadable at the Fire_cci website (<https://www.esa-fire-cci.org>, last accessed on September 2019), or through the CCI Open Data Portal (<http://cci.esa.int/data>, last accessed on September 2019).

2.2. Calibration sites

Ten calibration tiles were selected to develop the BA algorithm (Fig. 2). They were chosen as representatives of a wide range of vegetation types and fire regimes.

The first tile was located in the North Australian region (h30v10) where BA perimeters were available from the Northern Australian Fire Information (NAFI) (<http://www.firenorth.org.au/nafi3/>, last accessed on September 2019). This region is strongly dominated by tropical savanna in which fire is a fundamental management tool (Stroppiana et al., 2003). As an example of the boreal forest, two test tiles were located in Canada (h11v03 and h12v03), where the Canadian National Fire Database (CNFDB) provided BA perimeters for fires larger than 200 ha (<http://cwfis.cfs.nrcan.gc.ca/ha/nfdb>, last accessed on September 2019). As an example of temperate forests, a tile from the western coast of the United States was chosen (tile h08v05). The BA perimeters were downloaded from the Fire and Resource Assessment Program (FRAP) (<http://frap.fire.ca.gov/>, last accessed on September 2019).

Another six tiles (Fig. 2) were used for calibration purposes from areas that we previously identified as particularly problematic (Chuvieco et al., 2018). BA perimeters for those sites were not available, but we checked visually the different versions of the algorithm to assure that no major problems might arise. One of the problems checked in those tiles was the sensitivity of tile-based thresholds to different land covers (Angola, h19v10). Potential border effects were analysed between tiles in Central Africa (h19v07 and h19v08). A Kazakhstan tile (including regions of Uzbekistan and Turkmenistan) (h22v04) was selected as it may cause region-growing problems because of the high BA/HS ratio found in that area (Hantson et al., 2013). A tile in Colombia (h10v08) was chosen because of being a transition zone between grasslands and the Andean forest. Finally, a tile located in the Russian far eastern area (h25v03), in the north border with China, was selected, which is affected by huge fires almost every year during spring (Kobayashi et al., 2007).

All these tiles were used to visually control that algorithm results were reasonable, and no major problems were derived from the full processing. They were not used for validation purposes, but just to control the results of the different versions within the development of the algorithm.

2.3. Input data

The algorithm needs four input datasets to generate BA information. MOD09GQ (collection 6) product provides Terra's MODIS Red (620–670 nm) and NIR (841–876 nm) daily surface reflectance at 250 m spatial resolution (Vermote et al., 2015). This product also provides data quality information, but not state QA flags and viewing geometry. Therefore, we had to use the Terra's MOD09GA product as well, from which pixel state data was obtained (Table 1).

Active fire (hotspots or HS) information was obtained from the MODIS Global Monthly Fire Location Product, MCD14ML (collection 6) (<http://modis-fire.umd.edu/af.html>, last accessed on September 2019). This product contains descriptive information of each active fire, such as the geographic location and the date of detection. Both the thermal

Table 1
Summary of the state QA flag (Table 13: Vermote et al. (2015)).

Bit No.	Parameter name	Bit No.	Parameter name
0–1	Cloud state	11	Internal fire algorithm flag
2	Cloud shadow	12	MOD35 snow/ice flag
3–5	Land/water flag	13	Pixel is adjacent to cloud
6–7	Aerosol quantity	14	Salt pan
8–9	Cirrus detected	15	Internal snow mask
10	Internal cloud algorithm flag	—	—

bands that were used in the detection of these active fires (Giglio et al., 2016) and the state information coming from MOD09GA have a spatial resolution of 1 km (~ 16 pixels of 250 m), so the algorithm had to deal with the resolution difference to the MOD09GQ product. The process is detailed in the following sections.

Finally, the algorithm used standard land cover products to generate a burnable mask. The source of these data was the Land Cover CCI v2.0.7 (LC_CCI) product, which was developed within the CCI programme (<https://www.esa-landcover-cci.org/>, last accessed on September 2019). This LC_CCI product includes a year to year estimation of land cover, from 1992 to 2015, generated from different sensors (AVHRR, MERIS, SPOT ...) at 300 m resolution (ESA, 2017). This product was chosen over other global products for programme consistency, as well as because of similarities in temporal and spatial resolution. The burnable mask of each year was obtained by removing urban areas, bare areas, water bodies, and permanent snow and ice classes (Chuvieco et al., 2008; Simon et al., 2004).

2.4. Compositing

Although MODIS provides daily images of the entire globe, cloud contamination, cloud shadow, sensor failures or other reasons obviously affect the number of valid observations. One of the most common approaches to mitigating impacts of problems associated with daily images is the generation of temporal composites (Barbosa et al., 1998). Different compositing techniques can be found in the literature, which commonly enhances burned signal by maximizing or minimizing a specific spectral band (Chuvieco et al., 2005; Sousa et al., 2003). The aim of these techniques is to create noise-free images, with enough spatial coherence and where burned areas are emphasized. So, based on the previous versions experiences (Alonso-Canas and Chuvieco, 2015; Chuvieco et al., 2018), two criteria related to the closeness to the HS detection date and the minimum NIR value were applied to create monthly composites (NIR_t) (Fig. 4).

First of all, the nearest HS date was assigned to each pixel of the whole image based on a Thiessen matrix (Brassel and Reif, 1979). As MODIS active fire provides an accurate timing of the active fires (Boschetti et al., 2010), it can be used to establish the breakpoint between pre and post-fire images. To reduce border effects, a 50 km buffer was added to each tile, so HS near the border were included in the matrix calculation.

Considering that NIR reflectance is greatly reduced when areas are burned (Fraser et al., 2003; Pereira, 1999; Roy et al. 2002, 2005), minimizing NIR values was used as criterion for temporal compositing (Alonso-Canas and Chuvieco, 2015; Stroppiana et al., 2003; Zhang et al., 2003). However, low NIR values can also be caused by seasonal floods, cloud or topographic shadows. Therefore, state information was applied to each daily image in order to filter out clouds and cloud shadows (bit number 0–1, 2 & 10, Table 1). Besides, unburnable areas were not taken into account using the burnable mask.

The three lowest NIR values were obtained for each pixel and monthly period. The searching window included the pre-fire 10 days and post-fire 10 days, centred on the date established by the Thiessen matrix of HS dates, using previous and next month images, if necessary. When less than four valid observations were found after that date, an additional period of up to 15 post-fire days was searched to assure that enough post-fire valid observations were obtained (Fig. 3). If at least two of the three minimum values were detected in post-fire days, the closest to the HS date was selected. In any other case (i.e. when only one of the three minima was found in post-fire dates or the three minima were found in pre-fire dates), the second minimum was selected, as the first minimum was likely to be contaminated by cloud or topographic shadows that may have not been detected by the state mask. This second minimum was also selected when there were no active fires in that particular tile and period to create the Thiessen matrix. In this case, the searching window included the whole month.

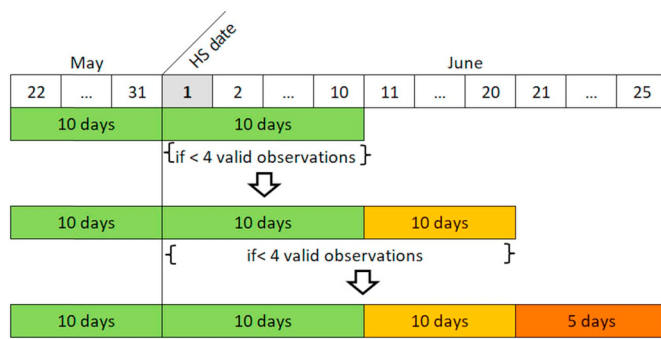


Fig. 3. Example of the three possible searching windows for the first day of June. The first case represents the standard one, where 20 (10 pre-fire and 10 post-fire) days were used. More post-fire days were added based on the availability of valid observations in the post-fire days.

The selected date for the monthly composite was used to retrieve the reflectance values for the following stages of the algorithm.

Since burned areas had a lower NIR value than unburned ones, a NIR decrease was noticeable after each fire event (Alonso-Canas and Chuvieco, 2015; Chuvieco et al., 2005; Pereira, 1999). The relative NIR drop ($\text{Rel}\Delta\text{NIR}_t$) was defined by the relative change between two consecutive composites (Fig. 4):

$$\text{Rel}\Delta\text{NIR}_t = \left(1 - \frac{\text{NIR}_t}{\text{NIR}_{t-1}}\right) \cdot 1000 \quad (1)$$

where NIR_t is the composite of the month being processed and NIR_{t-1} was the NIR value of the previous composite. The variable was multiplied by 1000 and converted to integer values for computational reasons. The higher the $\text{Rel}\Delta\text{NIR}_t$ was, the higher the probability of being a burned pixel. Several authors have pointed that relative changes better account for the variability of background spectral values between pixels and between dates due to different environmental factors (biome type, soil characteristics, etc.) than absolute changes (Eva and Lambin, 1998; Roy et al., 2002). The $\text{Rel}\Delta\text{NIR}_t$ was used in the thresholding and growing phase, but when anomalous values were found that criterion was not considered. This was observed to occur when NIR_{t-1} reflectance value was higher than 5000 (MODIS scaled value), as it was clearly associated with undetected clouds or snow.

2.5. Generation of HS clusters

Different algorithms have used tile-based thresholds to detect BA.

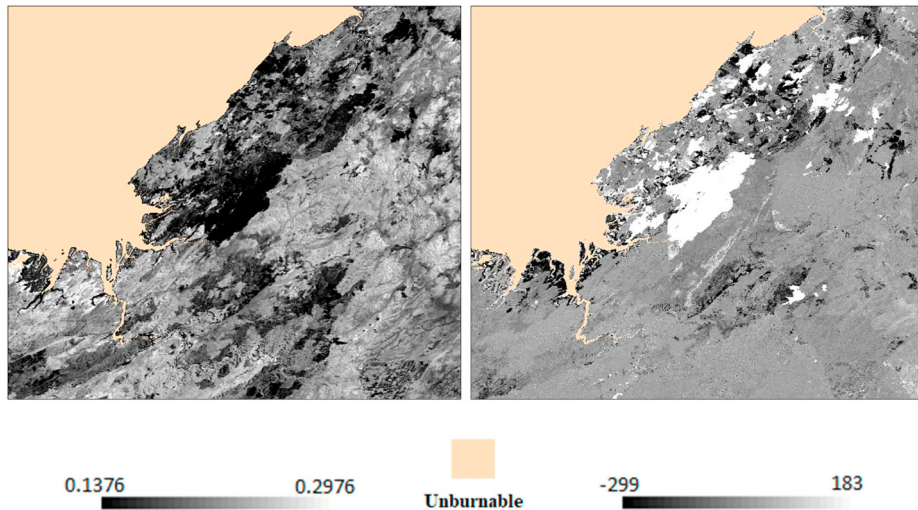


Fig. 4. NIR composite (left) and $\text{Rel}\Delta\text{NIR}$ (right) of a region of the tile h30v10 (North Australia).

They assume that regional statistics should be better adapted to the global diversity of fire conditions than applying single criteria (Alonso-Canas and Chuvieco, 2015; Chuvieco et al., 2018). However, tile-based approaches involve two difficulties: on one hand, tile thresholds may create border artefacts in areas with contrasting fire conditions, and on the other, they do not consider internal variations within tiles, which may be quite significant when tiles are very diverse in land cover or biomass conditions. To avoid those problems, instead of using tile-based thresholds our approach aimed to establish BA patch thresholds. For doing that, HS clusters were created considering both the spatial and temporal distribution of HS.

A spatial cluster (SC) was defined by those HS that were close enough in space. The radius of the area of influence (R_{AI}) of each HS was set up to 1875 m, based on findings of Hantson et al. (2013). These authors used a 1500 m buffer around the reference fire perimeters to assign HS to BA patches. To mitigate potential geolocation problems, 375 m were added to this value, to account for the neighbour pixels ($375 = 250 + 125$, as we had to consider the edges of those neighbouring pixels). HS with intersecting R_{AI} were considered part of the same SC (Fig. 5).

The temporal threshold to consider two HS as part of the same cluster was established at 4 days. Several authors have studied the influence of this time-gap parameter when defining fire patches. Archibald and Roy (2009), for example, used 4- and 8-day time-gaps in burned areas of savannah ecosystems. Oom et al. (2016) assessed the impact of using 2-, 8-, and 14-day time-gaps for fire event individuation based on active fires. More recently, Laurent et al. (2018) constructed a new global database of fire patch functional traits (FRY) where patches were created based on 3-, 5-, 9- and 14-day time-gap parameters. All of them concluded that smaller time-gaps led to a larger number of smaller fires, while larger time-gaps had the opposite effect. However, this effect was shown to be much more significant in tropical regions than in temperate or boreal regions (Oom et al., 2016). Based on this knowledge, a 4-day time-gap was chosen as it avoided creating too large HS clusters in tropical regions with high HS density while keeping large fires in boreal and temperate regions adequately represented.

Neighbour HS, i.e. those within the same SC, with a date difference longer than this period were considered as different fires, and were assigned to different spatio-temporal clusters (STC) (Fig. 5). To avoid artificial separation of STC and SC by monthly composites, we considered also HS of the previous month. Both the STCs and the SCs were the input units for the following phases of the BA algorithm.

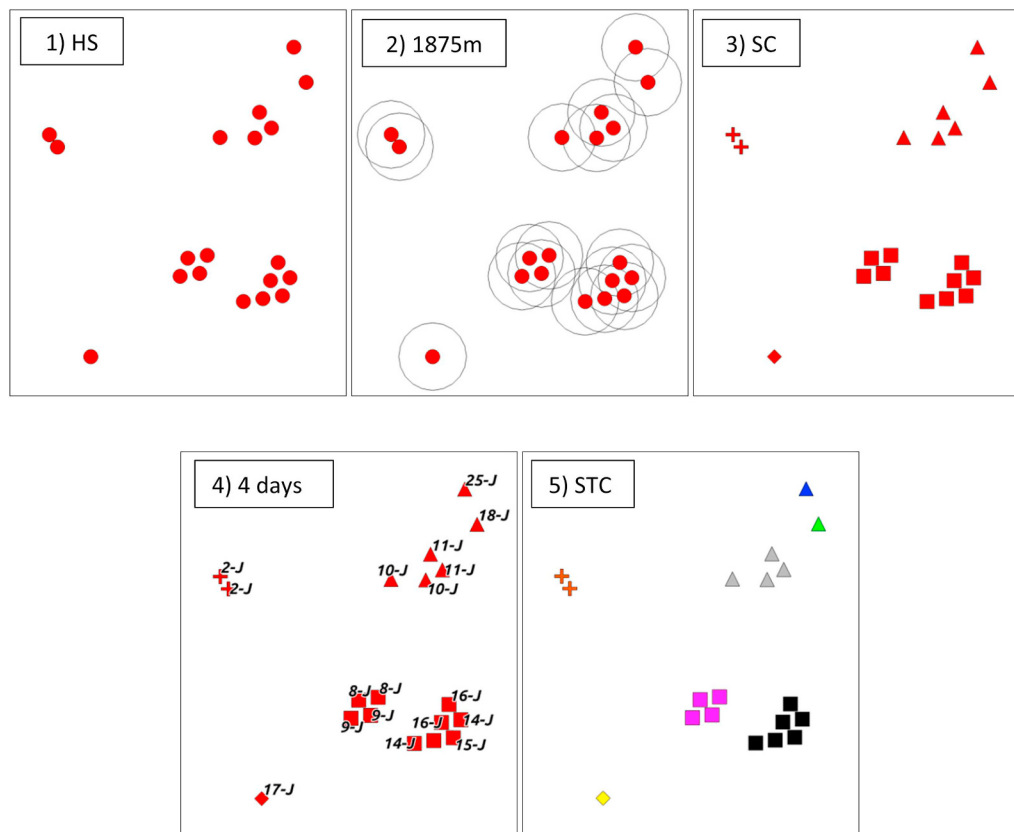


Fig. 5. Spatial clusters or SC (3) are derived by applying a spatial condition (2) to the HS (1). Each shape in (3) corresponds to different SC. Spatio-temporal clusters or STC (5) are generated when also the temporal condition (4) is applied. Each colour in (5) represents different STC within the same SC. (For interpretation of the references to colour in this figure legend, the reader is referred to the Web version of this article.)

2.6. Seed phase

2.6.1. Selection of Potential Active Fires (PAF)

This first step in the seed phase aimed to reduce commission errors by selecting only those pixels that had a high probability of being burned. Many authors have recommended using HS for this characterization (Alonso-Canas and Chuvieco, 2015; Fraser et al., 2000; Giglio et al., 2018; Roy et al., 1999), as HS tend to give an accurate identification and timing of active fires (Boschetti et al., 2010). However, some commission errors have been detected by several authors, particularly in regions with low fire occurrence (Hantson et al., 2013). HS may also be originated by fires smaller than the minimum detectable size of our input images (< 6.25 ha). In both cases, HS would not be associated with changes in the NIR reflectance. For these reasons, several authors proposed to filter out those HS that had not a significant change in NIR reflectance (Alonso-Canas and Chuvieco, 2015; Giglio et al., 2009).

On the other hand, HS are provided at 1×1 km resolution (≈ 16 pixels of 250 m). To improve the location of each active fire within that area, we selected the minimum NIR value of a 5×5 window around each HS coordinate (Fig. 6). The minimum NIR value was assumed to better represent actual burnings, as BA has low NIR reflectance and non-burnable covers had previously been filtered out (Section 2.4).

Once HS were located at 250 m, only those with a high probability of being burned were selected as Potential Active Fires (PAF). We included three conditions to classify a pixel as PAF: low values of NIR in the actual composite, high NIR changes from previous composite and spatial coherence.

The first condition was computed from the Cumulative Distribution Function (CDF) of the unburned class, in order to select a NIR threshold that would reduce the potential commission errors with unburned covers. The selection of the first decile to limit those potential commission errors to a maximum of 10% was first proposed by Alonso-Canas and Chuvieco (2015) and then ratified by Chuvieco et al. (2018).

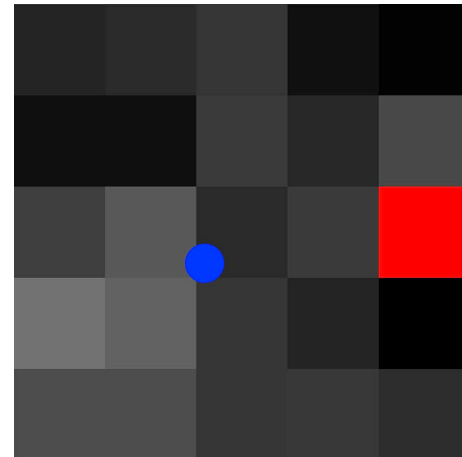


Fig. 6. The blue point in the centre is the original HS coordinate determined by the MCD14ML product and the red pixel is the estimated location of the HS at 250 m. (For interpretation of the references to colour in this figure legend, the reader is referred to the Web version of this article.)

The CDF of the unburned class was computed from all pixels located further than 10 km from any HS. This distance, termed R_1 , was established empirically after analysing fire patterns in the four calibration tiles with forest fire perimeters (Section 2.9).

The RelΔNIR between monthly composites aimed to remove those HS where the NIR value would not change significantly. This could occur in cases of fires burning a very small proportion of the MODIS pixel, or when HS would likely not be associated with biomass burning, such as those related to noise or undetected gas flares or power plants in the MCD14ML product. Previous versions established that any NIR decrease between the pre-fire and post-fire value was enough to consider an active fire as a probably burned pixel. However, this criterion

was not very selective, particularly in areas with high post-fire NIR values (hot soils or gas flares). Hence, we increased to 10% the Rel Δ NIR_t to classify an HS as PAF. This value was empirically obtained from the analysis of those calibration sites with more extension of bright soils, i.e. in the Northern Hemisphere Sub-Saharan Africa.

Finally, a spatial coherence test was included, by considering a certain number of pixels in the vicinity of each PAF.

In summary, the three conditions included to consider a HS as a PAF were:

1. NIR_t ≤ 10% of unburned CDF
2. Rel Δ NIR_t ≥ 10%
3. Three of the eight surrounding pixels (3 × 3 window) met conditions 1 and 2.

2.6.2. Establishing cluster-adapted thresholds

To better adapt spectral thresholds to the spatial variability of fire occurrence, they were obtained for each STC and SC previously established (Section 2.5).

The first threshold was derived by analysing burned and unburned pixels from the vicinity of each STC. The former was taken from the PAF included in each STC. The latter were selected from those pixels located within a strip that would fulfil two requirements: first to be close enough as to be sure the land cover was similar to the one burned, and second to be far enough as to be sure the pixels were not affected by the fire. This strip was found empirically to be between 10 (R_1) and 20 km (R_2) from each STC (Section 2.9). To avoid potential contamination of burned pixels, a buffer around each HS was excluded from the analysis. This buffer was defined by the R_{AI} previously computed (Fig. 7).

Then, a threshold for each STC was computed as:

$$TH_{STC,i} = \frac{1}{3} \cdot Med_{B,i} + \frac{2}{3} \cdot Mo_{U,i} \quad (2)$$

where $Med_{B,i}$ is the median of the burned sample and $Mo_{U,i}$ is the mode of the unburned one. The median and mode were used as they provided the best balance between omission and commission errors in the calibration sites where forest fire service perimeters were available, i.e. Australia, California, and Canada.

To improve the efficiency of the BA algorithm, two additional thresholds were computed, by taking into account the spatial relations among HS clusters. First, a SC threshold was derived from the thresholds of its STC members:

$$TH_{SC,j} = \frac{\sum_{i=1}^N \#PAF_i \cdot TH_{STC,i}}{\sum_{i=1}^N \#PAF_i} \quad (3)$$

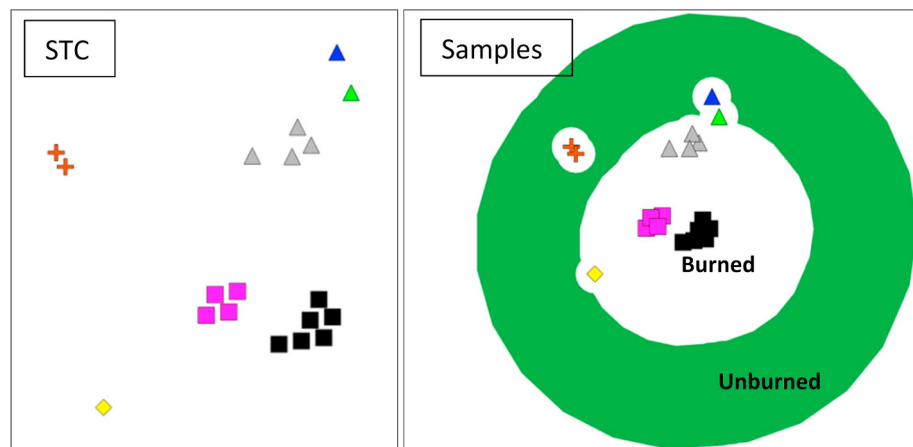


Fig. 7. Example of the burned and unburned samples for a specific spatio-temporal cluster (STC) represented by the black squares. The “holes” of the unburned sample corresponds to surrounding STCs R_{AI} which is removed to avoid unburned sample contamination by near BA.

where N is the number of STC within each SC_j and #PAF_i is the number of PAFs in each STC_i. Weighting by the number of PAFs we aimed to give more importance to larger fires within each SC.

Finally, a local threshold was computed for each SC by combining the thresholds of all SC located within R₂ (above mentioned). The same logic of weighted average was used:

$$TH_{LSC,k} = \frac{\sum_{j=1}^M \#PAF_j \cdot TH_{SC,j}}{\sum_{j=1}^M \#PAF_j} \quad (4)$$

where M is the number of SC within 20 km from each SC_k and #PAF_j is the number of PAFs in each SC_j.

These thresholds were computed for both variables (NIR_t and Rel Δ NIR_t). The final criteria to select the seed pixels were:

1. NIR_t ≤ TH_{LSC,k} NIR
2. Rel Δ NIR_t ≥ TH_{LSC,k} Rel Δ NIR

Fig. 8 shows the spatial variability of TH_{LSC,k} NIR for an area with high fire occurrence. The figure shows the relevance of considering local versus tile-based thresholds. A single NIR threshold for the whole tile would imply either omissions or commissions depending on the land cover affected by the fire and the actual fuel availability, while the spatio-temporal clusters approach provides very different NIR threshold values (from 0.12 to 0.20).

2.7. Growing phase

An iterative contextual growing based on local SC thresholds was applied to fully detect the burned patches and, thus, reduce omission errors. Contextual growing algorithms have shown more efficient when robust criteria are used to stop the iterative growing (Zhang et al., 2005). Our BA algorithm included three conditions:

1. NIR_t ≤ TH_{LSC,k} NIR (eq. (4))
2. Rel Δ NIR_t ≥ TH_{LSC,k} Rel Δ NIR (eq. (4))
3. An adjacent pixel in a “rook’s case” window (3 × 3) must be a seed or a pixel previously classified as burned.

2.8. Patch filtering

In order to avoid potential commission errors generated by excessive growing, the size and spatial distribution of the generated patches were taken into account (Alonso-Canas and Chuvieco, 2015). To detect and remove artefacts within detected patches a three-step filtering approach was applied (Fig. 9).

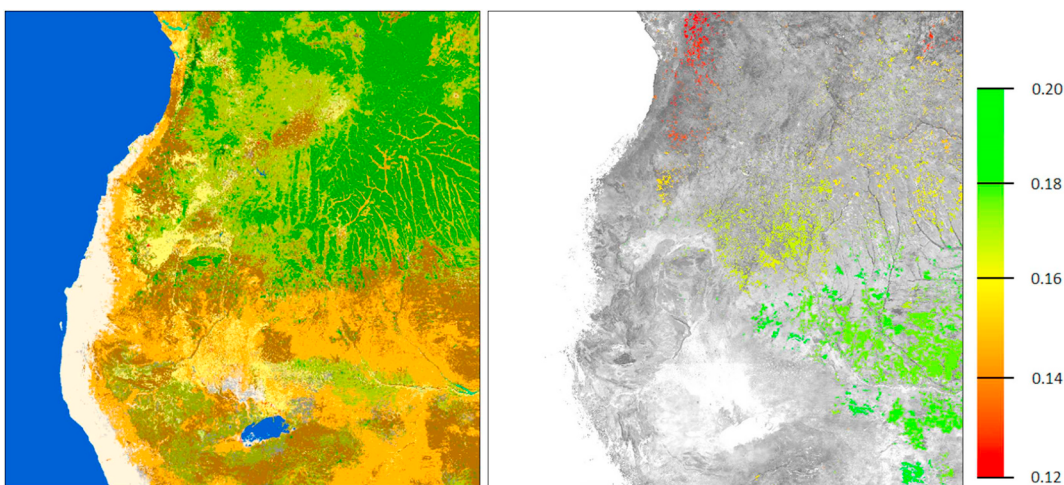


Fig. 8. Land cover CCI v2.0.7 of the year 2007 (a) and spatial variation of $\text{TH}_{\text{LSC},k}$ NIR (b) for September of 2008 of the tile h19v10 (Angola). Thresholds overlay the NIR composite.

A first criterion to detect and eliminate patches caused by artificial growing considered the number of burned pixels that were generated by each seed pixel (Fig. 9, F1). The full patch was removed from classification when this ratio exceeded 1000 pixels (62.5 km^2). We applied a conservative threshold to the maximum ratio found (Section 2.9), as other authors have found much lower values. For instance, Hantson et al. (2013) found a maximum size of $3.89 \text{ km}^2/\text{HS}$ for their analysis of different fire types, while Giglio et al. (2006) found a maximum value of $6 \text{ km}^2/\text{HS}$ for a northern hemisphere African area with low tree cover.

A second filter was applied to detect anomalous patterns for some patches that were observed that grew excessively towards areas of low NIR values. In this case, the criterion was that less than 10% of the burned pixels included in the patch were within R_{AI} (Fig. 9, F2). When this occurred, it was assumed that the growing was mostly caused by a neighbour low-reflectance unburned cover and the full patch was removed. This threshold was conservative as well (Section 2.9) and did not impact the correct detection of burned patches in areas with low HS density, such as the African savannas.

Finally, contiguous patches to burned areas were removed if they did not have associated HS, to avoid cases where burned patches were

falsely connected to unburned low-reflectance areas (Fig. 9, F3). This process was performed in two steps. First, the false connections between patches were removed and then those new patches without seeds were eliminated. The false connections were detected applying two criteria to every burned pixel:

- a) In a “rook’s case” window (3×3), both north and south pixels or both east and west pixels were unburned and,
- b) The burned pixel was further than R_{AI} of any seed.

The first condition considered as false connections only those of one-pixel thickness. The second one aimed to avoid eliminating small fires.

Finally, gaps along burned patches were filled to reduce omission errors by relabelling unburned pixels as burned if in a “rook’s case” window (3×3), both north and south pixels or both east and west pixels were burned. Those pixels finally classified as burned were dated with the day of the monthly composite image.

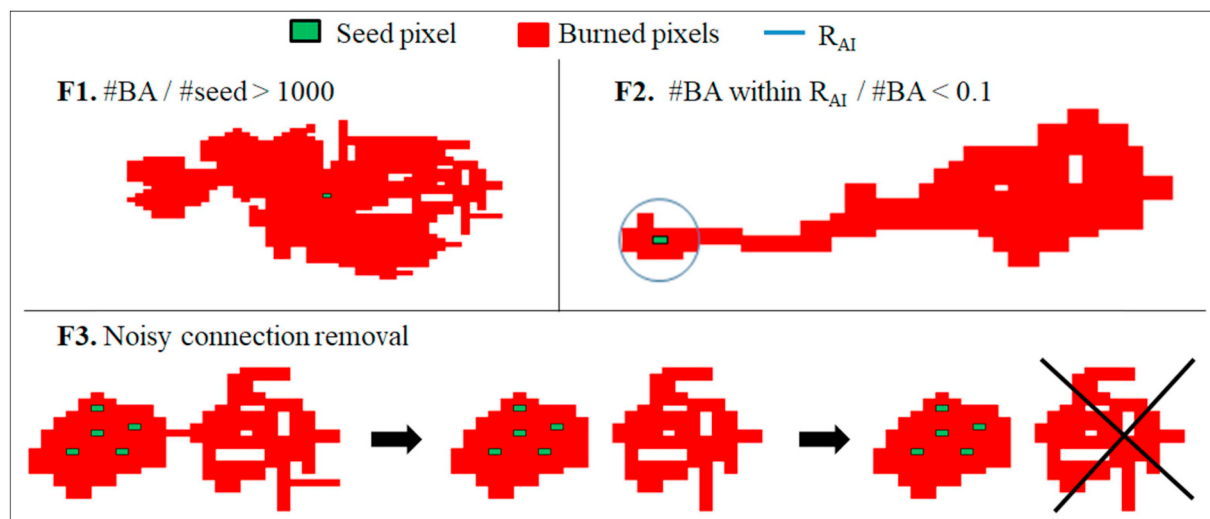


Fig. 9. Example of each fire patch removal and refinement filter. F1 shows how extreme growing is detected. F2 considered a situation in which too much burned area was found outside the area of influence ratio (R_{AI}), normally in a specific direction. F3 is the final refinement of patches in which noisy connections between BA and non-fire related areas are broken.

Table 2

Algorithm control parameters used by some steps indicated by Fig. 1.

Algorithm step	Parameter	Value	Description
Spatio-temporal clusters generation (Section 2.5)	Area of influence radius (R_{AI})	1875 m	The radius of the area of influence of each HS.
	Time-gap	4 days	Maximum detection date difference that can exist between HS that belong to the same HS cluster.
Potential Active Fires filtering (Section 2.6.1)	Unburned NIR CDF	10%	Maximum NIR value that can have a HS to be considered as PAF.
	Relative NIR drop	10%	Minimum NIR drop value that can have a HS to be considered as PAF.
Thresholding (Section 2.6.2)	First radius (R_1)	10 km	Minimum distance from the nearest HS where an unburned sample pixel can be found.
	Second radius (R_2)	20 km	Maximum distance from the nearest HS where an unburned sample pixel can be found.
Patch filtering (Section 2.8)	#BA/#seed	1000	Maximum number of burned pixels that can be generated by a single seed in a burned patch.
	#BA within R_{AI} /#BA	0.1	Minimum proportion of burned pixels that must be found within the R_{AI} of the HS of a burned patch.

2.9. Sensitivity analysis

Table 2 presents a summary of the parameters that control the behaviour of the algorithm, along with the step where they were used. Four of them were taken from findings of other papers, including previous versions of the algorithm. The other four parameters were derived empirically, based on the calibration sites. To analyse the robustness of the values finally selected, a sensitivity analysis was carried out by changing each of those empirical parameters around reasonable margins while keeping the other three constant. This exercise produced a set of 52 combinations of parameters, which implied the same number of classification outputs. We selected 2008 for this sensitivity analysis. Each classification was compared with the calibration perimeters of California, Australia, and Canada to measure the impact of each parameter in the final accuracy. Accuracy was estimated by the Dice coefficient (Fleiss et al., 2013), a metric previously used for assessment of BA products (Padilla et al., 2015).

Table 3 shows the results of this sensitivity analysis. Partial DC values from the three sites and the overall agreement is included. As a general comment, none of the parameters have a relevant impact on the DC, with overall values quite similar. However, higher differences are found in California, particularly with the radius. As expected, R_1 and R_2 , which were responsible for selecting the unburned sample, had more influence on the final results than the other two. These parameters that guided the patch filtering were used to detect anomalous cases (e.g. dark soils) in which the thresholding approach failed. Therefore, their influence is only noticeable in regions where those anomalous cases were found. For example, in the case of the BA proportion within R_{AI} , the DC value decreases 3% in California when the control parameter was not applied (value equal to 0).

All the final parameter's values were those that showed to be the most stable ones through the calibration tiles where fire perimeters

were available. The fact that the selected value was not the worst-case value in none of the calibration areas was considered important as well.

2.10. Validation

The results were validated using a sample of 1200 validation sites selected using a stratified random sampling (Padilla et al., 2018). Following a stage 3 validation procedure (<https://lpvs.gsfc.nasa.gov/index.html>, last accessed on September 2019), one hundred Landsat pairs per year were randomly selected, covering the period between 2003 and 2014. The sampling units were defined spatially following the Landsat Thiessen scene areas (TSA) (Cohen et al., 2010; Kennedy et al., 2010) and temporally using the dates of the available Landsat images. The strata were determined by the acquisition dates, biomes (Olson et al., 2001) and BA, using the MCD64A1 c5 product (Giglio et al., 2009), which was the best available when the project started. Reference burned perimeters were obtained from the multi-temporal comparison of Landsat TM or ETM + images using a semi-automatic classification procedure. First, the scenes were classified using a random forest classifier (Breiman, 2001; Pedregosa et al., 2011) and then visually supervised to refine the results. In order to ensure the good quality of the perimeters, the classification done by the interpreter was reviewed by another. The Landsat pairs used to generate the reference data were always acquired very close in time (maximum of 16 days, using both Landsat-5 and 7), to reduce potential BA omissions caused by the quick vegetation regrowth of some tropical areas.

Based on those reference perimeters and the derived error matrix (Congalton and Green, 1999), commission (Ce) and omission (Oe) errors, relative bias (relB) and Dice coefficient were calculated. The first two accuracy measures estimate undetected and over detected areas, respectively, while the relative bias determines error balance. The Dice coefficient (DC) (Fleiss et al., 2013) defines the probability of a classifier of detecting a pixel as burned taking into account that also the other classifies it as burned. The formulation of all this accuracy measures can be found in Padilla et al. (2015).

In addition to this global sample, another sample was derived for the African continent. In this case, the samples were generated to include a longer period to reduce the impacts of temporal reporting accuracy in the accuracy estimations. Thus, several consecutive Landsat pairs (each representing a maximum of 16 days period, termed short units) were interpreted and accumulated to generate long validation periods of up to 115 days (termed long units). This second sample was generated only for 2016, as it was initially developed for validating a Sentinel-2 BA product (Roteta et al., 2019). These African sampling units included 50 randomly selected sites. Approximately 1000 Landsat images were processed.

Table 3

Dice coefficients for different combinations of the BA algorithm parameters in three calibration sites. In bold the values used by the final version.

Parameter	Values	Canada	Australia	California	Total
First radius (R_1)	500 m	80.09%	82.22%	61.49%	81.69%
	10000 m	80.10%	82.46%	60.10%	81.83%
	20000 m	80.03%	82.50%	57.68%	81.79%
Second radius (R_2)	10000 m	80.03%	81.85%	60.75%	81.33%
	20000 m	80.04%	82.36%	61.15%	81.79%
	30000 m	80.13%	82.49%	59.76%	81.87%
#BA within R_{AI} /#BA	0	80.09%	82.36%	58.22%	81.71%
	0.1	80.09%	82.36%	61.25%	81.80%
	0.2	80.07%	82.31%	61.71%	81.76%
#BA/#seed	500	80.08%	82.28%	60.52%	81.70%
	1000	80.08%	82.37%	60.42%	81.78%
	1500	80.08%	82.38%	60.23%	81.79%

2.11. Intercomparison with existing products

Results obtained by our algorithm were compared with previous products generated within the same project as well as to existing global BA products. The selected products were the FireCCI41 (derived from MERIS data: Chuvieco et al. (2016)), FireCCI50 (based on a previous version of our algorithm: Chuvieco et al. (2018)) and the NASA's MCD64A1 c6 (based on 500 m MODIS data: Giglio et al. (2018)). Additionally, with the aim of analysing the sensitivity of each product to small fires the three MODIS products were compared with a BA product generated with Sentinel-2 data (at 20 m resolution) for Sub-Saharan Africa in 2016. This region was chosen as it covers around 70% of the global BA (Chuvieco et al., 2018; Giglio et al., 2018). The Sentinel-2 product for this region was named FireCCISFD11, and it was found more accurate than any global product for that region ($C_e = 19.3\%$ and $O_e = 26.5\%$) (Roteta et al., 2019).

2.12. Uncertainty characterization

Uncertainty characterization was required by the end-users of our project (mostly atmospheric and carbon modellers) since they require this information as input to their modelling efforts. Different authors have indicated that analytical propagation of errors through the algorithm is not feasible for threshold-based categorisation approaches (Merchant et al., 2017). Monte Carlo simulations or probability of output occurrence is recommended instead.

Logistic regression analysis was used to estimate BA probability as a surrogate of uncertainty characterization of the BA algorithm. The model was trained from the 10 calibration sites using data from 2008. Four input variables were included in the logistic models: monthly NIR composite (NIR), monthly relative NIR drop ($\text{Rel}\Delta\text{NIR}$), distance to the nearest BA seed (distance), and number of valid observations in the first 10 post-fire days (obs). The final coefficients derived from the logistic regression analysis were:

$$pB = \frac{1}{1 + e^c} \quad (5)$$

where pB is the BA probability and $c = -(3.533 - 0.01175 * \text{obs} - 0.001996 * \text{NIR} + 0.01417 * \text{Rel}\Delta\text{NIR} - 0.0009282 * \text{distance})$.

3. Results

3.1. Spatial and temporal trends

A time series of 18 years (2001–2018) was processed for 210 MODIS tiles that cover almost all the global burnable area (apart from some far north latitudes areas and very small islands). The results derived from the algorithm presented in this paper were formatted following the Fire_cci product specifications, generating a set of monthly GeoTIFF files with pixel results at 250 m, and a summary of burned areas at 0.25-degree cells in NetCDF format. The resulting product, named FireCCI51, indicates that an average of 4.63 Mkm^2 was burned globally (Fig. 10a), being 2004 the year with most burnings (5.19 Mkm^2) and 2001 the year with least (3.94 Mkm^2), although this year was influenced by having only one MODIS sensor to detect active fires, while the others have both Terra and Aqua acquisitions. Fig. 10b shows the most frequent fire peak months, that is, those that were identified in at least three of the 18 years, computed based on the grid product. Table 4 shows the burned area for each continental region (Giglio et al., 2006) in both percentage and km^2 and the values in which that contribution ranges throughout the time series.

The main global spatial trend clearly noticeable is the contribution of Sub-Saharan Africa to the global BA. An average of 68.5% of the global annual BA was located in Africa (3.16 Mkm^2). This area is almost equally distributed between Hemispheres: the Northern Hemisphere tropical region (NHAf) includes 32.7% of global BA, and the Southern

Hemisphere Africa (SHAF) covers 35.8%. In the NHAf region, fire especially affects the tropical savannahs of Central African Republic, Chad, and Sudan and has an insignificant presence on the Somalian bush-thickets region. In SHAF, the humid and dry Miombo and South African savannah are the most affected (Angola, the Democratic Republic of the Congo, Zambia, and Mozambique). Both regions burned during the dry season: from November to March in NHAf and from April to October months in SHAF.

The second major contributor to global BA is the northern tropical savannah of Australia (AUST), where an average of 0.48 Mkm^2 are burned annually (10.5% of total BA). This amount considerably increased in years 2001, 2011 and 2012 when more than 0.8 Mkm^2 of BA were detected, increasing global contribution to 21.33% in the first case. The peak month clearly matches the middle of the dry season (July) in the north and moves towards the south with the end of the dry season (October–November) (Fig. 10b).

A similar trend to Africa, but in a smaller proportion, is observed in South America. Northern hemisphere South America (NHSA), in addition to the southern hemisphere (SHSA), contribute on average 6.6% to the global BA (Fig. 10a). However, this contribution was greatly altered in the years 2007 and 2010 (10.8% and 11.7%, respectively) due to the “El Niño” phenomenon. Thus, the two South America regions ranged from below 0.2 Mkm^2 (e.g. 2009, 2013) to almost 0.6 Mkm^2 (e.g. 2007, 2010) during the time series. Like in Africa the north tropical savannahs burned during the dry season (January–March), mainly *Los Llanos* tropical grasslands in Colombia and Venezuela, while the fire season extends from July to September in SHSA, mostly in Brazil, followed by Bolivia, Paraguay, and Argentina. A subtle west-east direction of the fire season can be noticed in SHSA, mainly in the Cerrado tropical savannah in Brazil (Fig. 10b).

The Asian continent included an average of 11.7% of the global BA. Central Asia (CEAS) had an annual BA average of 0.24 Mkm^2 , which represents 5% of global BA. In this region, fire affects practically all the Russian southern border, and grasslands of Kazakhstan following the 50° parallel. Particularly interesting is the case of the Far East Russia (Amur region), where the border between Russia and China indicates a sharp change in BA. While the Russian area presents high fire activity, the Chinese northern region shows moderate activity, mostly related to agricultural burns. The Northern Plain of China also presents high fire activity. Four different patterns can be seen in the spatial distribution of the fires peak month through the region: April–May for north-western parts of Russia and from the north of Kazakhstan to Far East Russia, August for the south-western part (north Caucasus) of Russia, October for the China's north border agricultural areas, and June for the North China Plain. On the other hand, Boreal Asia (BOAS) and Southeast Asia (SEAS) similarly contribute to the global BA (Table 4). In the first case, large fires annually take place when the summer arrives at the highest latitudes. In the case of SEAS, a high fire occurrence peak can be found in February in Indochina that moves towards north preceding the arrival of the monsoon. A similar pattern can be distinguished in the agricultural areas of India, but one month later (March–April). The most affected countries in the area were Cambodia, Thailand, and Burma (Myanmar) (Fig. 10a).

The rest of the continental regions have significantly lower contributions to the global BA. In the temperate region of North America (TENA) some fire activity can be noted in the agricultural areas located at the Mississippi's alluvial plain and Central Great Plains, followed by the boreal areas (BONA). The average contribution of Central America (CEAM) and mainly the Mediterranean area of Europe (EURO) is similar, although the peak month changes from one to another (April–May and July–August, respectively) matching the warmest seasons.

3.2. Validation

The results of the global validation with the short-sampling units are

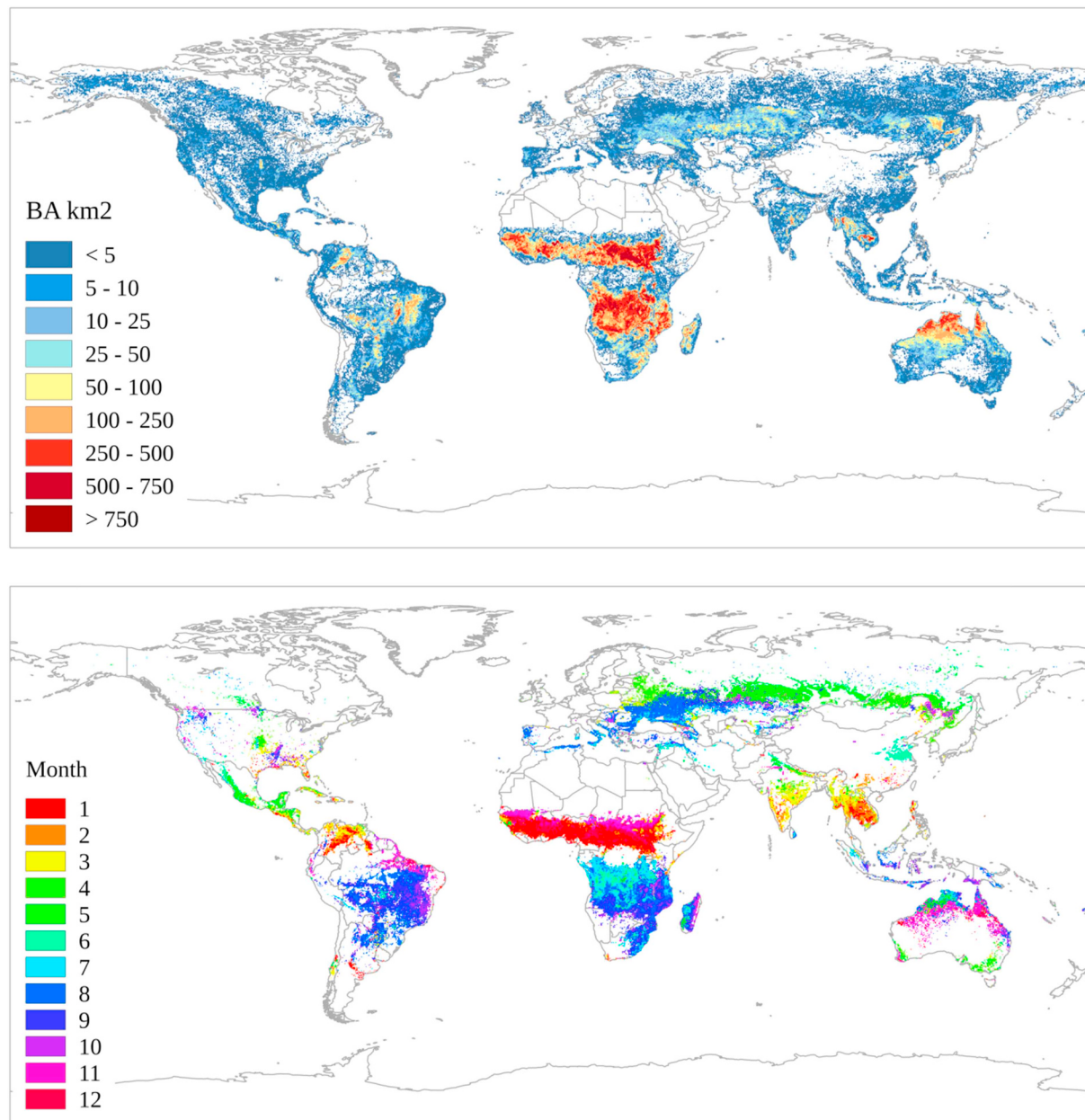


Fig. 10. Fire extent and seasonality obtained from the FireCCI51 product for the period 2001–2018. (a) Average global annual BA, and (b) the most frequent peak month (when frq > 3).

included in Table 5, which shows accuracy metrics for other BA products as well. The FireCCI51 had better commission and omission errors (10% and 14%, respectively) than the FireCCI41, which was based on MERIS data. This was expected due to the higher spatial and temporal resolution of the input data. Comparing the two versions of the MODIS products (FireCCI50 and FireCCI51) the latter offered a minor improvement in omission error (around 3%), with a similar increase in commission error. Relative bias was also improved, which implies a better equilibrium between over and underestimations. The Dice coefficient, which considers both types of errors, slightly improves in the latest Fire_cci product.

In these estimations of accuracy two errors are mixed: on one hand the thematic errors (burned/unburned pixels incorrectly classified) and, on the other, the reporting errors (pixels well detected but on different dates to the reference periods). When validation periods are longer, it is expected a lower impact of these reporting errors over the spatial accuracy estimates. For this reason, we also validated the Fire_cci

products using the sampling units generated for the African continent in 2016. Table 6 shows the accuracy metrics for both short and long sampling units for both MODIS products (FireCCI41 was not available for 2016, as the MERIS sensor was only operating until 2012). It was observed a significant decrease in both omission and commission errors for long sampling periods. The FireCCI51 had 25.8% fewer commission and 15.8% fewer omission errors than for the short sampling units, while the FireCCI50 had a lower but still significant improvement over short validation periods (24.9% in commission and 11.2% in omission errors). DC coefficients of the two products were also significantly higher for the long sampling units.

3.3. Reporting accuracy

A reporting accuracy analysis was made throughout all the calibration areas for the year 2008. The comparison was carried out using the MCD14ML product (which includes HS location and dates),

Table 4

Summary of the contributions of each continental region to the annual global burned area through the time series (2001–2018).

Code	Name	Global contribution			BA (km^2)		
		Average	Minimum	Maximum	Average	Minimum	Maximum
SHAF	Southern Hemisphere Africa	35.78%	26.14%	43.54%	1653829	1030845	1871717
NHAF	Northern Hemisphere Africa	32.67%	28.38%	36.95%	1510670	1278315	1885949
AUST	Australia and New Zealand	10.47%	4.00%	21.33%	482340	189637	841138
SHSA	Southern Hemisphere South America	5.46%	2.69%	10.57%	255507	118895	500692
CEAS	Central Asia	5.04%	2.25%	8.59%	235020	93413	395914
BOAS	Boreal Asia	3.51%	1.99%	6.56%	163101	80359	317581
SEAS	Southeast Asia	3.13%	1.75%	4.69%	144418	71832	194942
NHSA	Northern Hemisphere South America	1.18%	0.58%	1.61%	54279	29178	81069
TENA	Temperate North America	0.68%	0.36%	0.98%	31739	14175	47363
BONA	Boreal North America	0.55%	0.08%	1.05%	25136	3110	48863
CEAM	Central America	0.49%	0.26%	0.89%	23060	11367	45481
EURO	Europe	0.40%	0.21%	0.68%	18546	8191	26693
EQAS	Equatorial Asia	0.33%	0.09%	0.82%	15413	4345	36199
MIDE	Middle East	0.31%	0.16%	0.56%	14153	7009	24418

Table 5

Multiannual (2003–2014) estimated accuracy metrics of each Fire_cci product (Padilla et al., 2018). In parentheses standard errors of the estimates.

	DC	relB	Ce	Oe
FireCCI41	0.248 (0.030)	-0.468 (0.094)	0.643 (0.045)	0.810 (0.030)
FireCCI50	0.365 (0.026)	-0.402 (0.058)	0.512 (0.020)	0.708 (0.030)
FireCCI51	0.382 (0.025)	-0.280 (0.066)	0.544 (0.020)	0.671 (0.032)

computing the difference between this product and the detection date of both FireCCI50 and FireCCI51 (Fig. 11).

A total of 216,177 HS were analysed to determine the reporting accuracy of the FireCCI50 and 51 products. Both versions showed a practically equal amount of day of detection errors. 20.7% of the cases showed a very good agreement with the date established by the HS (0–1 days of difference), and 61.6% of the fires were reported with a 4 days accuracy. On the whole, more than 90% of the cases showed a reporting accuracy between 0 and 9 days, which supposed a slight improvement with respect to the FireCCI50.

3.4. Intercomparison with existing BA products

3.4.1. Intercomparison of spatial and temporal trends among existing products

Temporal trends showed an overall good global agreement between FireCCI51 and NASA MCD64A1 c6 products (Fig. 12). FireCCI51 had the highest amount of BA among the compared BA products, with an average annual BA of 4.63 Mkm^2 , followed by MCD64A1 c6 with 4.18 Mkm^2 (both for the period 2001–2018) and FireCCI50 with 3.81 Mkm^2 (for period 2001–2016). FireCCI51 and 50 had less BA in the first two years of the time series, because of partial gaps of MODIS HS caused by being acquired by a single satellite (Terra). After 2003, both Terra and Aqua MODIS data were used to acquire HS, hence the detected amount of BA clearly improved. MCD64A1 c6 was less affected by this issue as some parameters of the algorithm were modified to compensate for the lack of information in those years (Giglio et al., 2018). In any case, temporal trends of FireCCI51 agree with the rest of the BA products,

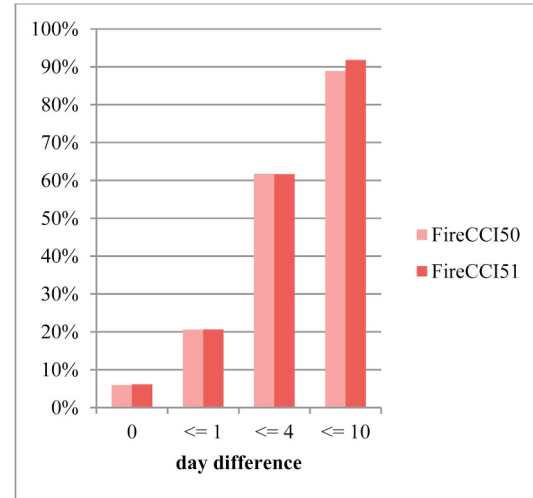


Fig. 11. Accumulated reporting accuracy of the FireCCI50 and FireCCI51 during the first 10 days after the fire.

including the peak of 2007 that was missed by FireCCI50.

Regarding the spatial patterns, all the products agree in the most affected regions (Fig. 13): NHAF and SHAF, although its relative contribution varies from 67.9% (MCD64A1 c6) to 74.6% (FireCCI41). In all cases, SHAF contributes more than the northern region, except for FireCCI41. The second most burned region was AUST in all products, although FireCCI41 was less sensitive to this area. FireCCI51 was found more sensitive to boreal fires than other products, having doubled the BA detections than other products, with almost 0.2 Mkm^2 burned annually. A similar pattern was observed in CEAS. Conversely, in SHSA the MCD64A1 c6 detected 0.03 Mkm^2 more BA than the FireCCI51.

3.4.2. Sensitivity to small fires detection

FireCCI50 (250 m), FireCCI51 (250 m) and MCD64A1 c6 (500 m) products were spatially compared to the FireCCISFD11 (20 m) product for Sub-Saharan Africa 2016 to analyse the sensitivity of each global

Table 6

Short unit and long unit (Africa, 2016) accuracy estimates (Padilla et al., 2018). In parentheses the standard errors of the estimates.

		DC	relB	Ce	Oe
Short unit	FireCCI50	0.318 (0.043)	-0.548 (0.078)	0.489 (0.044)	0.769 (0.041)
	FireCCI51	0.368 (0.039)	-0.388 (0.068)	0.515 (0.034)	0.703 (0.041)
Long unit	FireCCI50	0.473 (0.056)	-0.548 (0.078)	0.240 (0.029)	0.657 (0.058)
	FireCCI51	0.564 (0.041)	-0.388 (0.068)	0.257 (0.028)	0.545 (0.050)

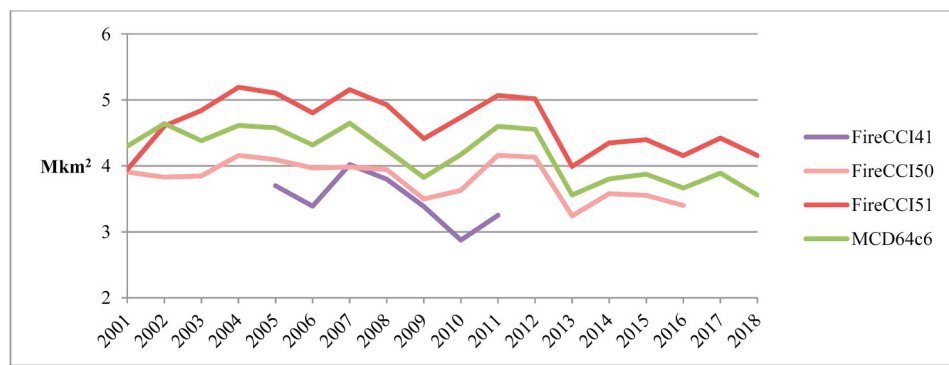


Fig. 12. Annual BA of ESA (FireCCI) and NASA (MCD64A1 c6) products.

product to detecting small fires. The FireCCISFD11 detected 4.9 Mkm² for the Sub-Saharan Africa, 60% more than the FireCCI51 (3.1 Mkm²), 80% more than the MCD64A1 c6 (2.7 Mkm²), and 97% more than the FireCCI50 (2.5 Mkm²).

Table 7 shows the monthly commission and omission errors of each MODIS product compared to FireCCISFD11. FireCCI51 was observed the most similar product, with an annual DC value of 0.42, followed by the FireCCI50 (DC = 0.38) and the MCD64A1 c6 (DC = 0.36). During high fire occurrence months, FireCCI51 showed the highest DC values with FireCCISFD11, followed by the FireCCI50 product. For low occurrence months MCD64A1 c6 had similar or slightly higher DC values than Fire_cci products. The lowest omission error for the FireCCI51 was found in December and June, while the highest was observed in the Spring (March–May). Conversely, the commission error was found lower and much more stable through the year ranging from 41% to 53%.

A monthly trend between DC and the total amount of BA detected for both hemispheres can be observed in Fig. 14. For the NHAF region, FireCCI51 was the most similar product to FireCCISFD11 in most months. MCD64A1 c6 showed a better agreement in low fire occurrence months (April–August) (Fig. 14a). For the SHAF, a similar trend was observed, with higher DC values for the June–September period (Fig. 14b). In both regions, the lowest occurrence months showed also the lowest DC values.

4. Discussion

4.1. FireCCI51 product assessment

This paper presents an improved version of a global BA algorithm

Table 7

Commission (Ce) and omission (Oe) errors calculated based on the comparison between the FireCCISFD11 and three BA MODIS products for Sub-Saharan Africa.

MONTH	FireCCI50		FireCCI51		MCD64A1 c6	
	C _e	O _e	C _e	O _e	C _e	O _e
January	46.5%	70.8%	49.7%	61.9%	54.1%	68.9%
February	50.0%	83.9%	52.0%	79.5%	60.4%	88.7%
March	45.9%	91.7%	44.6%	89.3%	53.9%	93.3%
April	44.0%	93.8%	47.5%	91.3%	62.0%	88.7%
May	53.4%	75.9%	53.2%	75.1%	59.6%	79.5%
June	49.0%	58.3%	47.0%	56.8%	44.8%	70.3%
July	45.4%	64.5%	45.3%	58.7%	42.9%	69.0%
August	43.5%	74.1%	42.2%	68.2%	42.8%	67.8%
September	47.5%	81.4%	46.5%	66.6%	39.8%	66.5%
October	47.0%	87.1%	41.9%	78.7%	51.1%	73.0%
November	38.2%	69.9%	41.9%	62.0%	43.2%	70.4%
December	42.8%	59.8%	43.8%	56.3%	46.3%	63.9%
Average	45.4%	72.9%	45.8%	66.5%	47.2%	71.7%

developed within the Fire_cci project. This algorithm tried to solve some of the issues observed in previous versions (FireCCI41: Chuvieco et al. (2016); FireCCI50: Chuvieco et al. (2018)), such as border effects, unexpected artefacts or underestimation related to low-intensity fires. The new product, named FireCCI51, offers a longer time series (2001–2018) than FireCCI41 (2005–2011) and FireCCI50 (2001–2016) at 250 m resolution, introduces new controls in the generation of spatial thresholds, improves the spatial coherency of burned patches and incorporates new a version of the land cover mask (Table 8).

At global scale, both validation and intercomparison results showed

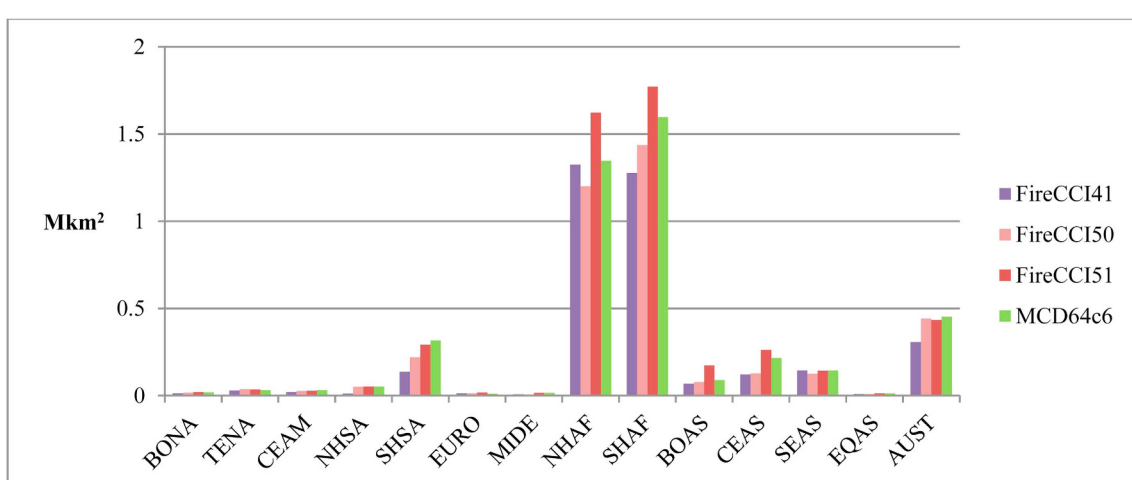


Fig. 13. Annual BA average in Mkm² for each continental region according to FireCCI41, FireCCI50, FireCCI51, and MCD64A1 c6, for the period 2005–2011.

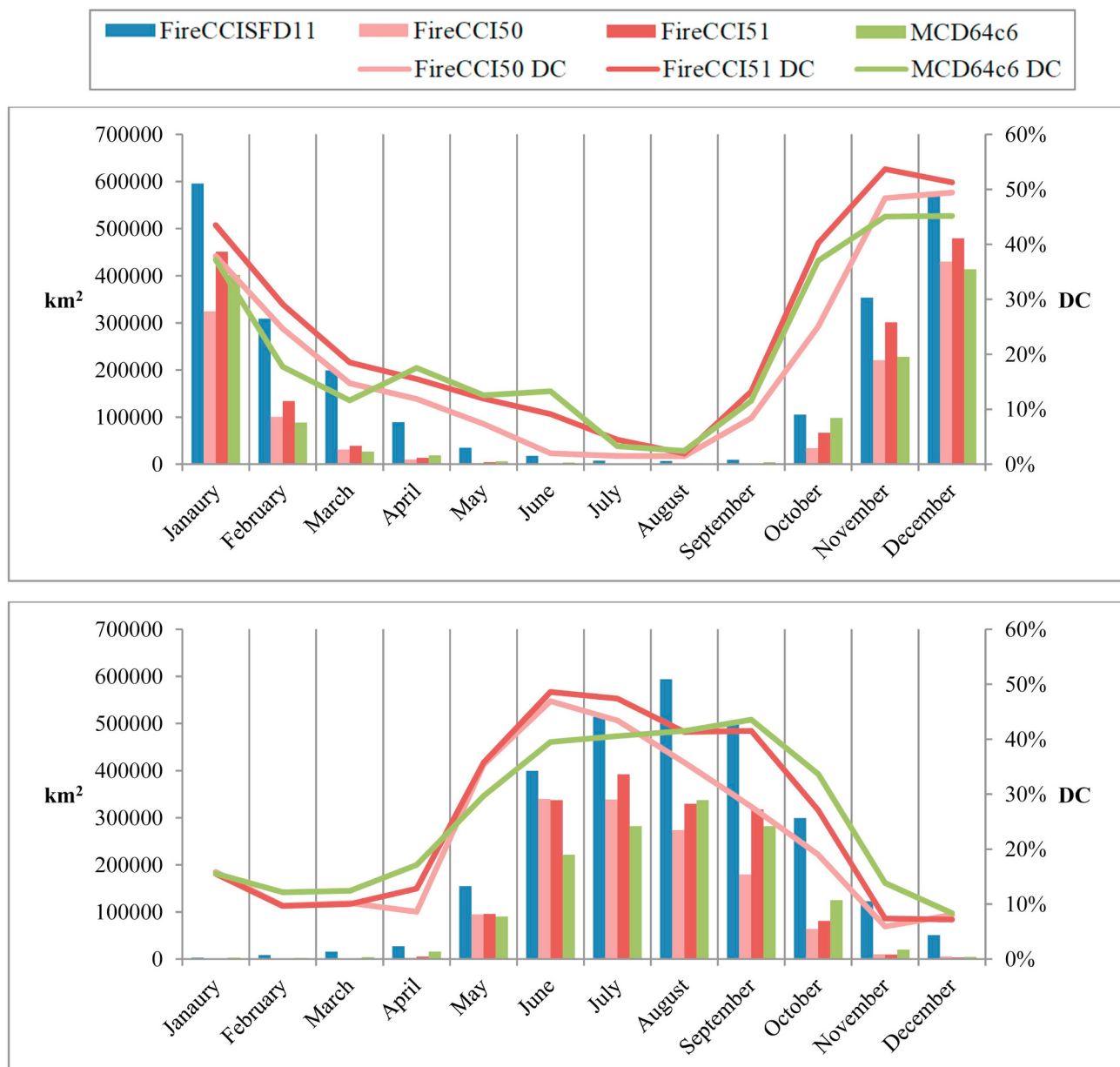


Fig. 14. Comparison of the MODIS BA products (FireCCI50, FireCCI51, and MCD64A1 c6) against the Sentinel-2 product (FireCCISFD11) for the year 2016. a) Northern Hemisphere Africa (NHAf) and b) Southern Hemisphere Africa (SHAf).

Table 8
Main differences among the Fire_cci global BA algorithms.

	FireCCI41	FireCCI50	FireCCI51
Input Reflectance	MERIS	MODIS c6	MODIS c6
Input HS	MODIS c5	MODIS c6	MODIS c6
Resolution	300 m	250 m	250 m
Land cover	LC_CCI v1.6.1	LC_CCI v1.6.1	LC_CCI v2.0.7
Time series	2005–2011	2001–2016	2001–2018
Compositing	HS date + NIR	HS date + NIR	HS date + NIR
Thresholding	Tile-based	Tile-based	Contextual-based
Reference	Alonso-Canas and Chuvieco (2015)	Chuvieco et al. (2018)	This paper

a better performance of the new algorithm over previous Fire_cci products, as FireCCI51 was found the most reliable product ($C_e = 54.4\%$, $O_e = 67.1\%$), followed by the FireCCI50 ($C_e = 51.2\%$, $O_e = 70.8\%$) and FireCCI41 ($C_e = 64.3\%$, $O_e = 81\%$). However, these errors are

strongly affected by the reporting accuracy of our product. We found that 92% of the burned pixels were detected within the first 10 days after the fire, but only 6% of the cases met exactly the fire date. Thus, short sampling units (< 16 days) would likely include errors related to detection dates, since well-detected burned pixels dated outside of the Landsat reference period were likely classified as either omission or commission errors. However, the long sampling units (covering more than 3 months) would be much less affected by this issue. In fact, the errors of FireCCI51 for long sampling units in Africa were significantly lower than for short-sampling units (reduction of 25% and 15% in commission and omission errors, respectively). For these sampling units, accuracy metrics for FireCCI51 were also higher than for other Fire_cci products.

On the other hand, the temporal and spatial trends of FireCCI51 showed a high agreement with existing global BA products. For the period 2001–2018, FireCCI51 had the higher average estimation of BA (4.63 Mkm²), which is 11% higher than the MCD64A1 c6 (4.18 Mkm²), 22% higher than FireCCI50 (3.81 Mkm²), and 33% higher than

FireCCI41 (3.49 Mkm², although this one refers to a shorter period: 2005–2011). At the continental scale, FireCCI51 was found more sensitive to boreal fires, with 75.4% higher estimations than MCD64A1 c6 in boreal Asia and 4.8% in boreal America. Previous assessments with existing global products observed a significant underestimation of BA in the boreal forest, particularly in central Russia (Humber et al., 2018). A recent paper also shows good agreement of our product with BA statistics for European temperate forest (Turco et al., 2019). On the contrary, FireCCI51 was found less sensitive (11% lower estimations) than MCD64A1 c6 in tropical and temperate fires in Southern Hemisphere South America.

In terms of global estimation of BA, the validation metrics of FireCCI51 showed an important underestimation of total BA, with higher omission than commission errors. This issue has also been observed in other global BA products (Alonso-Canas and Chuvieco, 2015; Chuvieco et al., 2018; Giglio et al. 2009, 2018; Roteta et al., 2019), and it has been attributed to the coarse spatial resolution of the input images, which implies missing small-size fires (< 100 ha) (Randerson et al., 2012; van der Werf et al., 2017). The recently released FireCCISFD11 product based on Sentinel-2A images at 20 m spatial resolution for the whole of Africa (Roteta et al., 2019) provided a unique opportunity to make an extensive comparison between coarse (250–500 m) and medium (20 m) resolution sensors to analyse their sensitivity to small fires detection. Using the same validation dataset, the FireCCISFD11 product was found more accurate than any global product for Africa, having 6.4% fewer commission errors and 28% less omission error than FireCCI51, and 1.1% fewer commission errors and 33% fewer omission errors than MCD64A1 c6 (Roteta et al., 2019). Since all these three products used the MODIS active fires to train the algorithms, the improvement in the BA detection of FireCCISFD51 should be mostly attributed to the spatial resolution of the input reflectance.

Using this Sentinel-2 BA product as the reference, the spatial agreement of FireCCI51 was found higher than for other global BA datasets, with a DC value of 0.42, and lower omission and commission. On a monthly basis, DC values increased when the burned area increased.

As an example of the global products' sensitivity to detecting small fires Fig. 15 shows an area in Western Congo, where small fires (mostly agricultural) are frequent. Although all global products missed most small burned patches, the FireCCI51 shows a higher detection rate than FireCCI50 and MCD64A1 c6. In any case, it is clear that products based on coarse resolution sensors have important limitations in areas where small fires are predominant.

4.2. Algorithm strengths and weaknesses

Our algorithm was based on just a single MODIS reflectance band (NIR), to take advantage of improved spatial resolution of this dataset (250 m), at the cost of reducing the potential benefits of using other spectral ranges, particularly the SWIR, which has been shown to be very sensitive to discriminate BA (Bastarrika et al., 2011; Giglio et al., 2018; Pereira, 1999). Focusing on NIR reflectance has the additional benefit of extending the range of sensors to which our algorithm should be suitable, as the vast majority acquire NIR reflectances (Landsat OLI, MODIS, Sentinel-2 MSI, Sentinel-3 OLCI, Envisat-MERIS, Proba-V ...). Hence continuity of the BA time series will be ensured by the new missions.

The MODIS wide scanning angle implies having strong BRDF effects at the extremes of the image swath. The compositing approach reduced the impacts of this problem, providing a more stable time series. In addition, it mitigated other potential confusions of BA with low-reflectance targets. However, the composition approach impacted the reporting accuracy of our product, which showed a moderate agreement between the dates of the HS and the detection date (> 90% within 10 days). Although the compositing method is able to provide a stable time series, this does not necessarily mean that the three NIR minima

have to be immediately after the HS date. The oscillation in reflectance produced by the BRDF may cause a displacement in the NIR minima selection. This displacement is strongly limited by the 10 post-fire days searching window. However, within those 10 days the selection of the three NIR minima may be greatly affected by the BRDF. Therefore, the finally selected NIR minimum date may not be the actual post-fire date, but a few days afterwards, depending on sensor geometry. Our criteria to create the temporal composites assure that the selected NIR value is the most sensitive to the burned signal, but not necessarily the most accurate date. Future test will be performed to refine the selection of the NIR minima dates by including multi-temporal trend approaches in the compositing criteria. Currently, the product provides a high discrimination ability within 10 days (90% of burn pixels), which should be suitable for most BA product users that work with monthly or annual datasets. Further improvements in retrieving the date of burning may be more important for atmospheric emission studies, or modellers that require daily estimations of BA.

The algorithm relied on the capacity of the composite to effectively enhance the burned signal. However, since the composite method was dependent on HS dates, the quality of HS detection impacted the overall process, as is the case of all hybrid algorithms. In our time series, it was noted the impact of using one or two satellites in the MODIS HS detections in the first years (2001–2003), since the Aqua acquisitions were only available in 2002. The Visible Infrared Imaging Radiometer Suite (VIIRS) sensor aboard Suomi-NPP satellite and Joint Polar Satellite System (JPSS) will be an alternative source of HS detections for future versions of the algorithm. In addition, a European HS product is foreseen to be obtained from the Sea and Land Surface Temperature Radiometer (SLSTR) aboard Sentinel-3.

The new contextual thresholding approach applied in this version of the algorithm improved the spatial adaptation of classification thresholds while reducing the dependence of having land cover information, commonly used in global BA algorithms (Giglio et al. 2009, 2018). Using land cover products to adapt algorithm behaviour have been shown to improve spatial thresholds but implies depending on land cover errors, which extends the uncertainty of the final BA product. The spatial clustering approach of our algorithm included indirectly that information by taking into account the values that were found in burned patches surrounding unburned areas, which are likely to be of the same vegetation class and fuel conditions that those affected by fires. When adapting the algorithm to other sensors special care should be given to the distances proposed in this paper. The R_{AI} (area of influence ratio) was based on the HS distribution and also took into account its detection resolution. Although the same distance could be applied with other sensors, an analysis of the HS distribution is suggested if the input active fire product is changed. In a similar way, it is important to control the unburned sample size derived from the contextual approach for each SC. The robustness of the mode as representative of unburned conditions should be tested when the algorithm is applied to other spatial resolutions.

It was observed that in large BA with low HS density (e.g. South African Savannahs) part of the unburned sample was contaminated by burned pixels. In those cases, SC of the same burned patch were separated by more than 20 km, so R₁ (10 km) discarded only part of the burned pixels. Although this situation was unusual, underestimation could be expected in those cases due to the calculation of too restrictive thresholds. This issue can be handled by increasing both R₁ and R₂ size only for those regions.

Another partial limitation of the algorithm was related to phenomena that had similar spectral behaviour to BA. High RelΔNIR values may be caused by land cover changes not associated with fire, such as flooding or ice melting in boreal regions. Although the use of HS information decreases this effect and the final patch filtering applied by the algorithm effectively overcomes that issue, special care is recommended in regions where those events (e.g. floods) occur in the surroundings of BA.

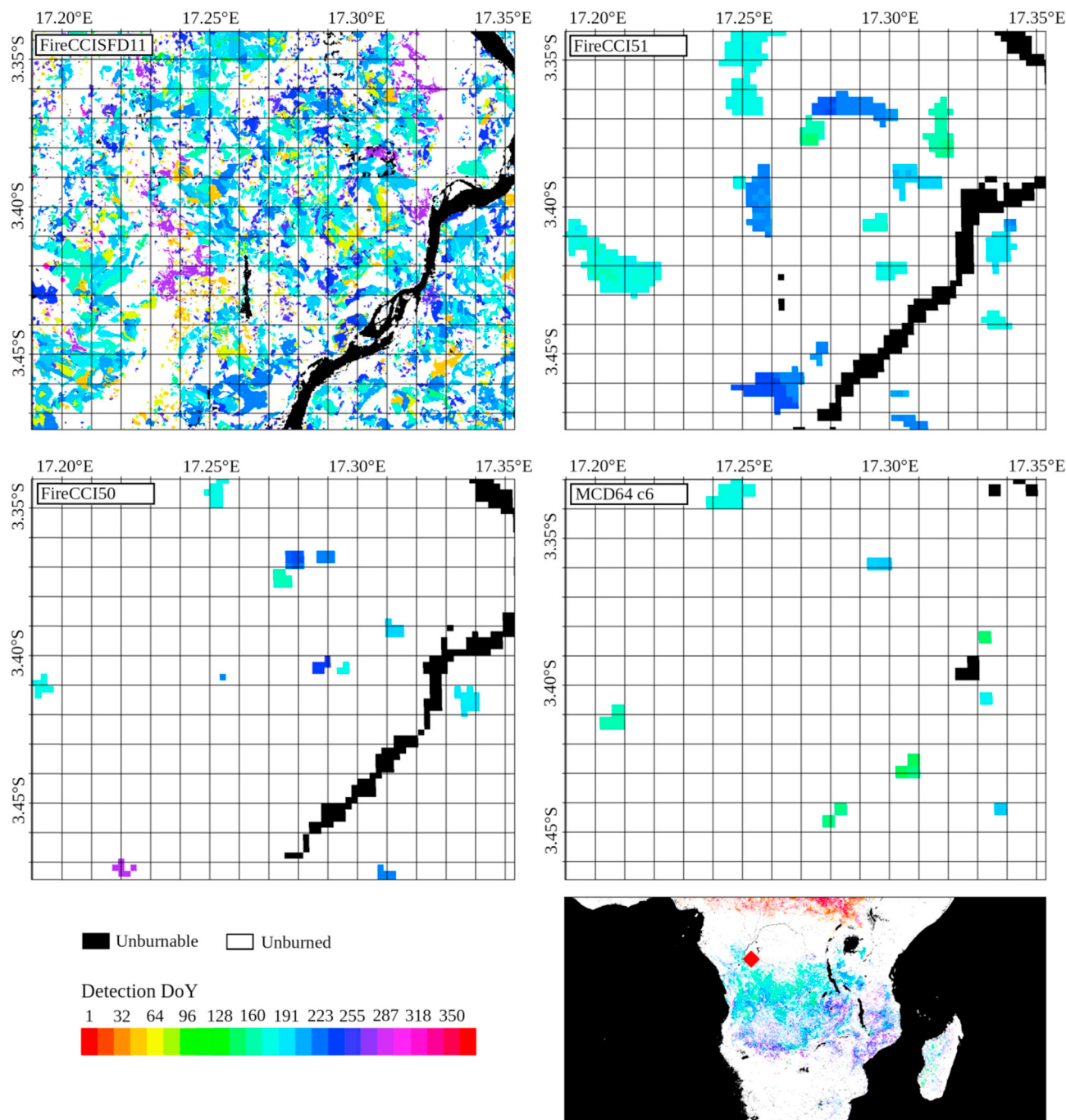


Fig. 15. Example of the sensitivity to the small fires of three global BA products: FireCCI50, FireCCI51, and MCD64A1 c6 compared to FireCCISFD11. This example is located in the Democratic Republic of Congo near the Equator where small fires are common.

5. Conclusions

This paper presents a hybrid BA algorithm that was developed within the Fire_cci project. It was based on MODIS thermal anomalies and MODIS NIR reflectances at 250 m resolution, improving the spatial resolution of existing global BA products. This algorithm was built upon the experience of a previous prototype (Chuvieco et al., 2018) to generate a long time series of BA datasets for the climate modelling community. A two-phase approach was used to detect BA. In the first step, only HS that have a high probability of being burned were selected, with the aim of reducing commission errors. In a second step, a contextual growing was applied from the seed pixels to reduce omission errors by detecting the whole burned patch. Both phases were based on

spatio-temporal clusters of active fires, which were used to derive detection thresholds better adapted to local fuel and fire conditions.

A full time series of 18 years (2001–2018) was processed to generate the FireCCI51 BA product. The annual BA average was 4.63 Mkm², which was 11% higher than the MCD64A1 c6 and 22% more than the previous version of the algorithm. However, the comparison carried out with a Sentinel-2 BA product derived for 2016 in Sub-Saharan Africa (FireCCISFD11) showed that both FireCCI51 and all others global BA products underestimate the total BA, emphasizing the need of using medium resolution sensors for generating global BA products. However, the FireCCI51 showed the highest similarity with the Sentinel-2 product from existing global BA datasets, particularly in terms of small fire detection capacity.

Reporting accuracy showed a moderate agreement between the dates of the HS and the detection date. This impacted the validation exercise that showed significantly higher accuracy estimates when using long validation periods (> 3 months).

The new algorithm was able to adapt adequately throughout different biomes and years. As it only relied on the near-infrared channel and thermal anomalies information, it has a high potential to be adapted to other coarse spatial resolution sensors, such as the OLCI sensor aboard Sentinel-3 or even to the new constellations of high-resolution satellites (Planet, Airbus).

Declaration of competing interest

The authors declare that they have no known competing financial interests or personal relationships that could have appeared to influence the work reported in this paper.

Acknowledgements

This study has been funded by the Fire_cci project (contract no 4000115006/15/I-NB), which is part of the European Space Agency's Climate Change Initiative Programme, and by the Spanish Ministry of Science, Innovation, and Universities through a FPU doctoral fellowship (FPU17/02438). The FireCCI51 dataset is freely available in both grid and pixel format through the Fire_cci website (<https://www.esa-fire-cci.org>, last accessed on September 2019), or through the CCI Open Data Portal (<http://cci.esa.int/data>, last accessed on September 2019). We thank Marc Padilla for carrying out the validation and Thomas Storm (Brockmann Consult GmbH) for processing the algorithm. We also thank Asier Badiola (Euskal Estatistika Erakundea, EUSTAT) for useful technical discussions.

References

- Alonso-Canas, I., Chuvieco, E., 2015. Global burned area mapping from ENVISAT-MERIS data. *Remote Sens. Environ.* 163, 140–152.
- Archibald, S., Lehmann, C.E., Gómez-Dans, J.L., Bradstock, R.A., 2013. Defining pyromes and global syndromes of fire regimes. *Proc. Natl. Acad. Sci.* 110, 6442–6447.
- Archibald, S., Roy, D.P., 2009. Identifying individual fires from satellite-derived burned area data. In: 2009 IEEE International Geoscience and Remote Sensing Symposium, pp. III-160–III-163.
- Barbosa, P.M., Pereira, J.M.C., Grégoire, J.M., 1998. Compositing criteria for burned area assessment using multitemporal low resolution satellite data. *Remote Sens. Environ.* 65, 38–49.
- Bastarrrika, A., Chuvieco, E., Martín, M.P., 2011. Mapping burned areas from Landsat TM/ETM+ data with a two-phase algorithm: balancing omission and commission errors. *Remote Sens. Environ.* 115, 1003–1012.
- Bird, M., Cali, J., 1998. A million-year record of fire in sub-Saharan Africa. *Nature* 394, 767.
- Bojinski, S., Verstraete, M., Peterson, T.C., Richter, C., Simmons, A., Zemp, M., 2014. The concept of essential climate variables in support of climate research, applications, and policy. *Bull. Am. Meteorol. Soc.* 95, 1431–1443.
- Bond, W.J., Keeley, J.E., 2005. Fire as a global 'herbivore': the ecology and evolution of flammable ecosystems. *Trends Ecol. Evol.* 20, 387–394.
- Boschetti, L., Flasse, S., Trigg, S., JACQUES DE DIXMUDE, A., 2002. A Multitemporal Change-Detection Algorithm for the Monitoring of Burnt Areas with SPOT-Vegetation Data. Analysis of Multi-Temporal Remote Sensing Images (Pp. 75-82). World Scientific.
- Boschetti, L., Roy, D.P., Justice, C.O., Giglio, L., 2010. Global assessment of the temporal reporting accuracy and precision of the MODIS burned area product. *Int. J. Wildland Fire* 19, 705–709.
- Bowman, D.M.J.S., Balch, J.K., Artaxo, P., Bond, W.J., Carlson, J.M., Cochrane, M.A., D'Antonio, C.M., DeFries, R.S., Doyle, J.C., Harrison, S.P., Johnston, F.H., Keeley, J.E., Krawchuk, M.A., Kull, C.A., Marston, J.B., Moritz, M.A., Prentice, I.C., Roos, C., Scott, A., Swetnam, T., Van der Werf, G., Pyne, S.J., 2009. Fire in the Earth system. *Science* 324, 481–484.
- Brassel, K.E., Reif, D., 1979. A procedure to generate Thiessen polygons. *Geogr. Anal.* 11, 289–303.
- Breiman, L., 2001. Random forests. *Mach. Learn.* 45, 5–32.
- Cohen, W.B., Yang, Z., Kennedy, R., 2010. Detecting trends in forest disturbance and recovery using yearly Landsat time series: 2. TimeSync — tools for calibration and validation. *Remote Sens. Environ.* 114, 2911–2924.
- Congalton, R.G., Green, K., 1999. Assessing the Accuracy of Remotely Sensed Data: Principles and Applications. Lewis Publishers, Boca Raton.
- Chuvieco, E., Lizundia-Loiola, J., Pettinari, M.L., Ramo, R., Padilla, M., Tansey, K., Mouillet, F., Laurent, P., Storm, T., Heil, A., 2018. Generation and analysis of a new global burned area product based on MODIS 250 m reflectance bands and thermal anomalies. *Earth Syst. Sci. Data Discuss.* 512, 1–24.
- Chuvieco, E., Mouillet, F., van der Werf, G.R., San Miguel, J., Tanasse, M., Koutsias, N., García, M., Yebra, M., Padilla, M., Gitas, I., Heil, A., Hawbaker, T.J., Giglio, L., 2019. Historical background and current developments for mapping burned area from satellite Earth observation. *Remote Sens. Environ.* 225, 45–64.
- Chuvieco, E., Opazo, S., Sione, W., Del Valle, H., Anaya, J., Di Bella, C., Cruz, I., Manzo, L., López, G., Mari, N., González-Alonso, F., Morelli, F., Setzer, A., Csizsar, I., Kanpandegi, J.A., Bastarrika, A., Libonati, R., 2008. Global burned land estimation in Latin America using MODIS composite data. *Ecol. Appl.* 18, 64–79.
- Chuvieco, E., Ventura, G., Martín, M.P., Gomez, I., 2005. Assessment of multitemporal compositing techniques of MODIS and AVHRR images for burned land mapping. *Remote Sens. Environ.* 94, 450–462.
- Chuvieco, E., Yue, C., Heil, A., Mouillet, F., Alonso-Canas, I., Padilla, M., Pereira, J.M., Oom, D., Tansey, K., 2016. A new global burned area product for climate assessment of fire impacts. *Glob. Ecol. Biogeogr.* 25, 619–629.
- Ershov, D., Novik, V., 2001. Mapping Burned Areas in Russia with SPOT4 VEGETATION (S1 Product) Imagery. Final Report for the Joint Research Centre of the European Commission, contract 07-F01EI.
- ESA, 2017. Land cover CCI product user guide version 2. Tech. Rep Available at: http://maps.elie.ucl.ac.be/CCI/viewer/download/ESACCI-LC-Ph2-PUGv2_2.0.pdf.
- Eva, H., Lambin, E.F., 1998. Burnt area mapping in Central Africa using ATSR data. *Int. J. Remote Sens.* 19, 3473–3497.
- Fleiss, J.L., Levin, B., Paik, M.C., 2013. Statistical Methods for Rates and Proportions. John Wiley & Sons.
- Forkel, M., Dorigo, W., Lasslop, G., Teubner, I., Chuvieco, E., Thonicke, K., 2017. A data-driven approach to identify controls on global fire activity from satellite and climate observations (SOFIA V1). *Geosci. Model Dev. (GMD)* 10, 4443.
- Fraser, R.H., Fernandes, R., Latifovic, R., 2003. Multi-temporal mapping of burned forest over Canada using satellite-based change metrics. *Geocarto Int.* 18, 37–47.
- Fraser, R.H., Li, Z., Cihlar, J., 2000. Hotspot and NDVI Differencing Synergy (HANDS): a new technique for burned area mapping over boreal forest. *Remote Sens. Environ.* 74, 362–376.
- Giglio, L., Boschetti, L., Roy, D.P., Humber, M.L., Justice, C.O., 2018. The Collection 6 MODIS burned area mapping algorithm and product. *Remote Sens. Environ.* 217, 72–85.
- Giglio, L., Loboda, T., Roy, D.P., Quayle, B., Justice, C.O., 2009. An active-fire based burned area mapping algorithm for the MODIS sensor. *Remote Sens. Environ.* 113, 408–420.
- Giglio, L., Schroeder, W., Justice, C.O., 2016. The collection 6 MODIS active fire detection algorithm and fire products. *Remote Sens. Environ.* 178, 31–41.
- Giglio, L., Van der Werf, G., Randerson, J., Collatz, G., Kasibhatla, P., 2006. Global estimation of burned area using MODIS active fire observations. *Atmos. Chem. Phys.* 6, 957–974.
- Hantson, S., Padilla, M., Corti, D., Chuvieco, E., 2013. Strengths and weaknesses of MODIS hotspots to characterize global fire occurrence. *Remote Sens. Environ.* 131, 152–159.
- Hantson, S., Pueyo, S., Chuvieco, E., 2016. Global fire size distribution: from power law to log-normal. *Int. J. Wildland Fire* 25, 403–412.
- Hollmann, R., Merchant, C.J., Saunders, R.W., Downy, C., Buchwitz, M., Cazenave, A., Chuvieco, E., Defourny, P., Leeuw, G.D., Forsberg, R., Holzer-Popp, T., Paul, F., 2013. The ESA Climate Change Initiative: satellite data records for essential climate variables. *Bull. Am. Meteorol. Soc.* 94, 1541–1552.
- Humber, M.L., Boschetti, L., Giglio, L., Justice, C.O., 2018. Spatial and temporal inter-comparison of four global burned area products. *Int. J. Digit. Earth* 1–25.
- Kasischke, E., French, N.H., 1995. Locating and estimating the areal extent of wildfires in Alaskan boreal forest using multiple-season AVHRR NDVI composite data. *Remote Sens. Environ.* 51, 263–275.
- Kaufman, Y.J., Remer, L.A., 1994. Detection of forests using Mid-IR reflectance: an application for aerosol studies. *IEEE Trans. Geosci. Remote Sens.* 32, 672–683.
- Kennedy, R.E., Yang, Z., Cohen, W.B., 2010. Detecting trends in forest disturbance and recovery using yearly Landsat time series: 1. LandTrendr — temporal segmentation algorithms. *Remote Sens. Environ.* 114, 2897–2910.
- Kobayashi, M., Nemilostiv, Y.P., Zyryanova, O.A., Kajimoto, T., Matsuura, Y., Yoshida, T., Satoh, F., Sasa, K., Koike, T., 2007. Regeneration after forest fires in mixed conifer broad-leaved forests of the Amur region in far eastern Russia: the relationship between species specific traits against fire and recent fire regimes. *Eurasian J. For. Res.* 10, 51–58.
- Laurient, P., Mouillet, F., Yue, C., Ciais, P., Moreno, M.V., Nogueira, J.M., 2018. FRY, a global database of fire patch functional traits derived from space-borne burned area products. *Sci. Data* 5, 180132.
- Mason, P., Zillman, J., Simmons, A., Lindstrom, E., Harrison, D., Dolman, H., Bojinski, S., Fischer, A., Latham, J., Rasmussen, J., 2010. Implementation plan for the global observing system for climate in support of the UNFCCC (2010 Update). In: Citeseer.
- Merchant, C.J., Paul, F., Popp, T., Ablain, M., Bontemps, S., Defourny, P., Hollmann, R., Lavergne, T., Laeng, A., de Leeuw, G., 2017. Uncertainty information in climate data records from Earth observation. *Earth Syst. Sci. Data* 9.
- Mouillet, F., Schultz, M.G., Yue, C., Cadule, P., Tansey, K., Ciais, P., Chuvieco, E., 2014. Ten years of global burned area products from spaceborne remote sensing—a review: analysis of user needs and recommendations for future developments. *Int. J. Appl. Earth Obs. Geoinf.* 26, 64–79.
- Olson, D.M., Dinerstein, E., Wikramanayake, E.D., Burgess, N.D., Powell, G.V.N., Underwood, E.C., D'amico, J.A., Itoua, I., Strand, H.E., Morrison, J.C., Loucks, C.J., Allnutt, T.F., Ricketts, T.H., Kura, Y., Lamoreux, J.F., Wettenberg, W.W., Hedao, P., Kassem, K.R., 2001. Terrestrial ecoregions of the world: a new map of life on Earth.

- Bioscience 51, 933–938.
- Oom, D., Silva, P., Bistinas, I., Pereira, J., 2016. Highlighting biome-specific sensitivity of fire size distributions to time-gap parameter using a new algorithm for fire event individuation. *Remote Sens.* 8, 663.
- Padilla, M., Stehman, S.V., Hantson, S., Oliva, P., Alonso-Canas, I., Bradley, A., Tansey, K., Mota, B., Pereira, J.M., Chuvieco, E., 2015. Comparing the accuracies of remote sensing global burned area products using stratified random sampling and estimation. *Remote Sens. Environ.* 160, 114–121.
- Padilla, M., Wheeler, J., Tansey, K., 2018. ESA CCI ECV Fire Disturbance: D4.1.1. Product Validation Report, version 2.1. Tech. Rep. https://www.esa-fire-cci.org/sites/default/files/Fire_cci_D4.1.1_PVR_v2.1_0.pdf.
- Pedregosa, F., Varoquaux, G., Gramfort, A., Michel, V., Thirion, B., Grisel, O., Blondel, M., Prettenhofer, P., Weiss, R., Dubourg, V., 2011. Scikit-learn: machine learning in Python. *J. Mach. Learn. Res.* 12, 2825–2830.
- Pereira, J.M.C., 1999. A comparative evaluation of NOAA/AVHRR vegetation indexes for burned surface detection and mapping. *IEEE Trans. Geosci. Remote Sens.* 37, 217–226.
- Randerson, J., Chen, Y., Werf, G., Rogers, B., Morton, D., 2012. Global burned area and biomass burning emissions from small fires. *J. Geophys. Res.: Biogeosciences* 117 – G04012 (2005–2012), 1–23.
- Roteta, E., Bastarrika, A., Padilla, M., Storm, T., Chuvieco, E., 2019. Development of a Sentinel-2 burned area algorithm: generation of a small fire database for sub-Saharan Africa. *Remote Sens. Environ.* 222, 1–17.
- Roy, D., Jin, Y., Lewis, P., Justice, C., 2005. Prototyping a global algorithm for systematic fire-affected area mapping using MODIS time series data. *Remote Sens. Environ.* 97, 137–162.
- Roy, D., Lewis, P.E., Justice, C.O., 2002. Burned area mapping using multi-temporal moderate spatial resolution data—a bi-directional reflectance model-based expectation approach. *Remote Sens. Environ.* 83, 263–286.
- Roy, D.P., Giglio, L., Kendall, J.D., Justice, C.O., 1999. Multi-temporal active-fire based burn scar detection algorithm. *Int. J. Remote Sens.* 20, 1031–1038.
- Seiler, W., Crutzen, P.J., 1980. Estimates of gross and net fluxes of carbon between the biosphere and the atmosphere from biomass burning. *Clim. Change* 2, 207–247.
- Silva, J.M.N., Sousa, A.M.O., Pereira, J.M.C., Tansey, K., J.-M, G., 2002. A contribution for a global burned area map. In: Viegas, D.X. (Ed.), *IV International Conference On Forest Fire Research. 2002 Wildland Fire Safety Summit* (P. 13). Millpress, Luso, Coimbra, Portugal.
- Simon, M., Plummer, S., Fierens, F., Hoelzemann, J.J., Arino, O., 2004. Burnt area detection at global scale using ATSR-2: the GLOBSCAR products and their qualification. *J. Geophys. Res. Atmos.* 109, D14S02. <https://doi.org/10.1029/2002JD003622,1-16>.
- Sousa, A.M.O., Pereira, J.M.C., Silva, J.M.N., 2003. Evaluating the performance of multitemporal image compositing algorithms for burned area analysis. *Int. J. Remote Sens.* 24, 1219–1236.
- Stroppiana, D., Grégoire, J.M., Pereira, J.M.C., 2003. The use of SPOT VEGETATION data in a classification tree approach for burnt area mapping in Australian savanna. *Int. J. Remote Sens.* 24, 2131–2151.
- Tansey, K., Grégoire, J.M., Defourny, P., Leigh, R., Peckel, J.F., Bogaert, E.V., Bartholome, J.E., 2008. A new, global, multi-annual (2000–2007) burnt area product at 1 km resolution. *Geophys. Res. Lett.* 35, L01401. <https://doi.org/10.1029/2007GL03156>.
- Tansey, K., Grégoire, J.M., Stroppiana, D., Sousa, A., Silva, J., Pereira, J.M., Boschetti, L., Maggi, M., Brivio, P.A., Fraser, R., Flasse, S., Ershov, D., Binaghi, E., Graetz, D., Peduzzi, P., 2004. Vegetation burning in the year 2000: global burned area estimates from SPOT VEGETATION data. *J. Geophys. Res. Atmos.* 109, D14S03. <https://doi.org/10.1029/2002JD003598,2-22>.
- Turco, M., Herrera, S., Tourigny, E., Chuvieco, E., Provenzale, A., 2019. A comparison of remotely-sensed and inventory datasets for burned area in Mediterranean Europe. *Int. J. Appl. Earth Obs. Geoinf.* 82, 101887.
- van der Werf, G.R., Randerson, J.T., Giglio, L., van Leeuwen, T.T., Chen, Y., Rogers, B.M., Mu, M., van Marle, M.J.E., Morton, D.C., Collatz, G.J., Yokelson, R.J., Kasibhatla, P.S., 2017. Global fire emissions estimates during 1997–2016. *Earth Syst. Sci. Data* 9, 24.
- Vermote, E., Roger, J., Ray, J., 2015. MODIS Surface Reflectance User's Guide-Collection 6. Tech. Rep. Version 1.4, NASA GSFC Terrestrial Information Systems Laboratory, MODIS Land Surface Reflectance Science Computing Facility. Greenbelt, USA.
- Zhang, Q.F., Pavlic, G., Chen, W.J., Fraser, R., Leblanc, S., Cihlar, J., 2005. A semi-automatic segmentation procedure for feature extraction in remotely sensed imagery. *Comput. Geosci.* 31, 289–296.
- Zhang, Y.-H., Wooster, M., Tubutalina, O., Perry, G., 2003. Monthly burned area and forest fire carbon emission estimates for the Russian Federation from SPOT VGT. *Remote Sens. Environ.* 87, 1–15.